

Geochemical Barriers in CO₂ Capture and Storage Feasibility Studies

Barbara Cantucci · Giordano Montegrossi · Mauro Buttinelli ·
Orlando Vaselli · Davide Scrocca · Fedora Quattrocchi

Received: 31 October 2013 / Accepted: 13 September 2014 / Published online: 25 September 2014
© Springer Science+Business Media Dordrecht 2014

Abstract CO₂ sequestration in geological formations requires specific conditions to safely store this greenhouse gas underground. Different geological reservoirs can be used for this purpose, although saline aquifers are one of the most promising targets due to both their worldwide availability and storing capacity. Nevertheless, geochemical processes and fluid flow properties are to be assessed pre-, during, and post-injection of CO₂. Theoretical calculations carried out by numerical geochemical modeling play an important role to understand the fate of CO₂ and to investigate short-to-long-term consequences of CO₂ storage into deep saline reservoirs. In this paper, the injection of CO₂ in a deep structure located offshore in the Tyrrhenian Sea (central Italy) was simulated. The results of a methodological approach for evaluating the impact that CO₂ has in a saline aquifer hosted in Mesozoic limestone formations were discussed. Seismic reflection data were used to develop a reliable 3D geological model, while 3D simulations of reactive transport were performed via the TOUGHREACT code. The simulation model covered an area of >100 km² and a vertical cross-section of >3 km, including the trapping structure. Two simulations, at different scales, were carried out to depict the local complex geological system and to assess: (i) the geochemical evolution at the reservoir–caprock interface over a short time interval, (ii) the permeability variations close to the CO₂ plume front, and (iii) the CO₂ path from the injection well throughout the geological structure. One of the most important results achieved in this study was the formation of a geochemical barrier as CO₂-rich acidic waters flowed into the limestone reservoir.

B. Cantucci (✉) · M. Buttinelli · F. Quattrocchi
Istituto Nazionale di Geofisica e Vulcanologia, Via Vigna Murata 605, 00141 Rome, Italy
e-mail: barbara.cantucci@ingv.it

G. Montegrossi · O. Vaselli
CNR - IGG, Via G. La Pira 4, 50121 Florence, Italy

O. Vaselli
Dipartimento di Scienze della Terra, Università degli Studi di Firenze, Via G. La Pira 4,
50121 Florence, Italy

D. Scrocca
CNR - IGAG, P.le A. Moro 5, 00185 Rome, Italy

As a consequence, a complex precipitation/dissolution zone formed, which likely plays a significant role in the sequestration of CO₂ due to either the reduction of the available storage volume and/or the enhancement of the required injection pressure.

Keywords CO₂ geological storage · Reactive transport modeling · Deep saline aquifers · Geochemical barriers · Permeability feedback

1 Introduction

Carbon capture and storage (CCS) is a promising technology able to stabilize and reduce the atmospheric concentration of anthropogenic CO₂ by storing this greenhouse gas underground above critical PT conditions, i.e., 7.3×10^6 Pa and 31 °C (Metz et al. 2005, 2007; IEA 2009). This technique requires the capture of CO₂ from industrial flue gas plant and the subsequent injection, after compression, into suitable deep geological formations (Holloway 1996; Metz et al. 2005; IEA 2009), such as those containing saline aquifers, depleted oil, and gas fields, and deep non-exploitable coal beds. The geological storage of CO₂ in deep-seated saline aquifers is estimated to have a large potential capacity (350–1,000 Gt CO₂; Holloway 2001). Such reservoirs are relatively common worldwide (Hitchon et al. 1999; Gunter et al. 2000), thus incrementing the probability to locate the injection site close to major CO₂ anthropogenic sources and reducing the CO₂ transportation costs (Soong et al. 2004; Allen et al. 2005; Zerai et al. 2006).

In order to minimize the possible risks associated with this technology and to ensure a safe storage of CO₂ at depth, potential seepages and leakages as well as other geological hazards such as seismicity and natural degassing have to carefully be evaluated (e.g., Pruess and García 2002; Rosebaum et al. 2002; Rutqvist and Tsang 2002; Damen et al. 2006; Jones et al. 2006; Quattrocchi et al. 2008; Voltattorni et al. 2009).

During pre-feasibility studies, direct measurements of the targeted reservoir are limited, and reopening of closed deep wells, if present, may be expensive and not worthwhile. For a safe and appropriate use, accurate geological, hydrogeological, geochemical, and geomechanical investigations of the target area are a fundamental pre-requisite.

The injection sites need to satisfy the following requirements: (i) stable geodynamic environments of the hosting geological structures, (ii) safe and economically convenient depths (800–2,500 m) of the hosting saline aquifers, (iii) absence of seismogenic sources and areas, (iv) absence of historical and recent seismic events, (v) absence of diffuse degassing structures, (vi) absence of thermal anomalies, (vii) presence of anthropogenic CO₂ sources close to the storage site to reduce transport costs (Bumb et al. 2009; Duncan 2009).

In 2009, the European Council adopted a directive (2009/31/EC) to enable environmentally safe CCS where the assessment criteria to evaluate the suitability of a geological formation for CO₂ storage were specified. According to these criteria, preliminary site selection is also expected to identify extent, timing, and impact of the CO₂ plume migration on the basis of reactive processes.

A preliminary assessment of the reservoir evolution during and after the CO₂ injection can be accomplished by means of numerical simulations of both geochemical and fluid flow processes. Despite the fact that assumptions and limitations are necessarily introduced in these theoretical calculations, reactive transport modeling is one of the few approaches allowing to investigate short-to-long-term consequences of CO₂ storage and to evaluate the efficiency of trapping mechanisms (i.e., physical, hydrodynamic, and geochemical trapping; Gunter et al. 1993, 2000, 2004). Hydrodynamic and geochemical processes responsible

for CO₂ trapping mechanisms over large time frames have extensively been studied (e.g., Johnson et al. 2001; Bachu and Adams 2003; Gunter et al. 2004; Xu et al. 2004, 2005, 2007; Audigane et al. 2008). However, performing numerical simulations of a full coupling multiphase, multi-component fluid flow with kinetic geochemical reactions is still challenging because of Central Processing Units (CPU) time and memory constraints, especially when considering pertinent mineralogical assemblage (Nghiem et al. 2004; Gaus et al. 2008). To overcome such limitations, simplified 1D or 2D geological models were generally used in reactive transport simulations (e.g., Xu et al. 2005). Alternative procedures such as streamline-based simulations (i.e., Obi and Blunt 2006) or integrated approach coupling geochemistry and reservoir simulations (i.e., Klein et al. 2013) were proposed to simulate fine-grid model and to reduce the computing time.

A further challenge in reactive transport simulations is the feedback between geochemical reactions and fluid flow. Reactions among host rock, aquifer fluid, and CO₂ may indeed induce variations in permeability and effective porosity, which can significantly affect the storage capacity of the geological reservoir. Rock dissolution can enhance effective porosity and permeability, although mineral precipitation is expected to act in an opposite way (e.g., Lichtner 1996; Xu et al. 2004; Izgec et al. 2007). This process is amplified when carbonate systems are considered as they are characterized by fast kinetic reactions and deposition of secondary calcite, which can cause a significant decline of the initial permeability. Thus, composition of formation waters, initial permeability, temperature, flow rate, and injection period are to be considered (e.g., Izgec et al. 2005; Moghadasi et al. 2005). Feedbacks between transport and chemistry are important (Raffensperger 1996), although a large computational effort is required when modeled explicitly (Xu et al. 1999). Porosity changes are often monitored during simulations from changes in mineral volume, neglecting its effect on fluid flow (e.g., Xu et al. 2007; Schaefer et al. 2010).

Several studies were carried out to identify potential storage reservoirs in Italy (e.g., Donda et al. 2011; Buttinelli et al. 2011; Procesi et al. 2013). According to these investigations, an offshore carbonatic reservoir, located in central Italy, was selected to assess the suitability for CO₂ storage, during the pre-feasibility phase of the site investigation. The main goal was to evaluate the geochemical impact of CO₂ injection in a carbonatic structure by considering the porosity and permeability feedback on the fluid flow. Particular attention was given to geochemical processes inside and outside the CO₂ plume, since understanding the conditions in which dissolution and precipitation occur is a key-factor for assessing the evolution of porosity and permeability, the variation in the injectivity, and the efficiency of short-to-long-term trapping mechanisms.

Two numerical simulations were performed at different scale using the TOUGHREACT code: (i) a 3D simplified model representing a “column” centered in the injection well and (ii) a 3D large-scale model including the whole structure, from the sea floor to the reservoir bottom. The former was performed to investigate the CO₂–brine–mineral interaction at medium term (i.e., 100 years) in the reservoir and in the caprock. The latter was carried out to assess the effects of mineral dissolution/precipitation processes on both permeability and porosity changes and CO₂ flow path throughout the geological structure.

2 Regional Setting, CO₂ Injection Site and Geological Model Construction

Italy is located in an active and complex geodynamical domain characterized by the convergence between two major tectonic plates (Africa and Eurasia). This process has led to the formation of double-verging arcuate mountain chains (the Alps and the Apennines) in

association with the development of foredeep, fore-arc, and back-arc basins (e.g., [Horvath and Berckheimer 1982](#); [Dewey et al. 1989](#); [Carminati et al. 2004](#) and references therein). The presence of shallow and deep seismicity, anomalous heat flow, magmatism along the peri-Tyrrhenian margin, and several Diffuse Degassing Structures (DDS) ([Cataldi et al. 1995](#); [Chiodini et al. 1995, 2000](#); [Minissale 2004](#); [Chiarabba et al. 2005](#)) reflects the active geodynamic processes acting in the Italian peninsula.

Seismogenic areas are mostly located along the Alpine and Apennine chains, whereas DDS are distributed along the peri-Tyrrhenian margin, both representing the main geological risk factors for CO₂ geological storage ([Buttinelli et al. 2011](#) and references therein).

Schematically, the main geodynamic features recognizable in Italy are (e.g., [Scrocca et al. 2003](#) and references therein) as follows:

- (i) a foreland domain, represented by the Apula-Adriatic areas, characterized by Meso-Cenozoic passive margin sedimentary covers made up by turbiditic, evaporites, and shallow and deep carbonatic sequences;
- (ii) the Alps and Apennines, two distinct orogens, developed since Cretaceous and Eocene-Oligocene to the present, respectively;
- (iii) the Alpine and Apenninic foredeeps, where Pliocene-Pleistocene silico-clastic units overlie the Meso-Cenozoic passive margin sequences, often affected by several buried thrust-related folds;
- (iv) the Tyrrhenian back-arc basin where, over a stretched crust, a horst (mainly made up by limestone and Paleozoic metamorphic rocks) and graben (where thick silico-clastic units accumulated) architecture developed.

Numerous deep wells were drilled (mainly in the '80s) in the sedimentary basins for hydrocarbon exploration. The log data coupled with those related to shallow and deep seismic reflection lines provided basic information for recognizing the geological structures potentially hosting hydrocarbons, although most of them were only characterized by saline aquifers. Nevertheless, they can now be regarded as the main target for the geological storage of CO₂ (e.g., [Donda et al. 2011](#); [Buttinelli et al. 2011](#)).

The available well data and 2D multi-channel seismic profiles allowed to identify the presence of many promising areas suitable for CO₂ storage ([Buttinelli et al. 2011](#)). These areas are generally consisting of a thick and low permeability cover lying above a deep (>800 m) reservoir, in areas not affected by seismogenic structures and DDS ([Buttinelli et al. 2011](#)). Among the potential areas, a deep structure (about 1,900 m b.s.l.), located offshore in the eastern side of the Tyrrhenian Sea back-arc basin (i.e., Northern Latium offshore), was selected for the present study.

The structural setting of the study area and its tectonic evolution are characterized by alternating structural highs and lows (narrow elongated basins), with preferential NW–SE and subordinate N–S and E–W alignments. The stratigraphic setting is consisting of Upper Triassic evaporites, Jurassic to Cretaceous, mainly calcareous, successions, and Cretaceous–Oligocene turbiditic sandstones ([Fazzini et al. 1972](#)). Two major sedimentary cycles were recognized for the post-orogenic sequence: the Miocene to Middle Pliocene Lower (with subordinate semi-autochthonous units) and the Middle Pliocene to Quaternary Upper ([Bartole 1984, 1990, 1995](#); [Buttinelli et al. 2014](#)) cycles (Fig. 1).

The interpretation of the available well and seismic reflection data (e.g., [Buttinelli et al. 2014](#)) suggested that the selected site detains the necessary prerequisites (namely a massive caprock above a deep saline aquifers) for CO₂ storage and an estimated static storage capacity ranging from 52 to 228 Mt ([Procesi et al. 2013](#)). [Procesi et al. \(2013\)](#) showed that the injection of CO₂ for 20 years in the selected structure would be able to reduce the emission of CO₂ in

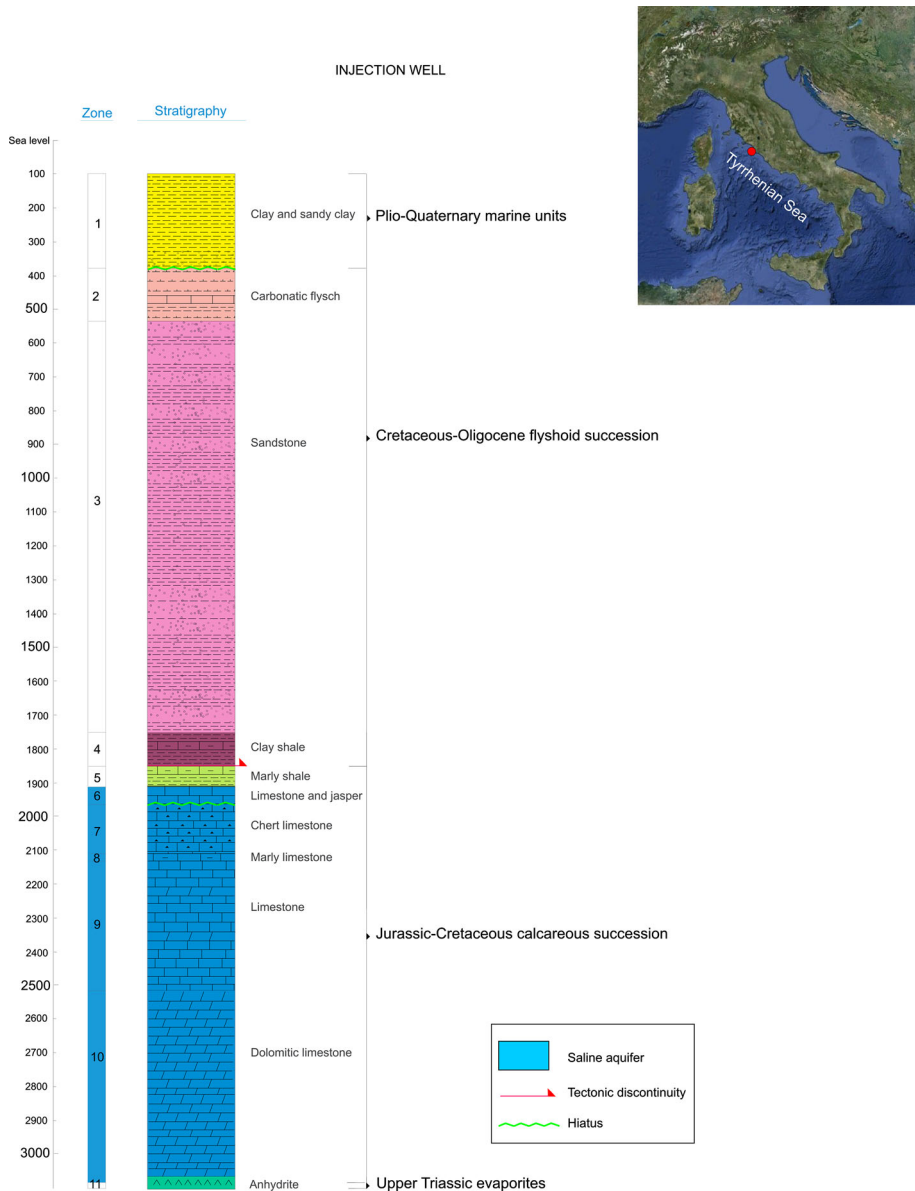


Fig. 1 Location of the potential injection site (red circle) and the respective simplified stratigraphic column. In the numerical models, the structure was divided in 11 zones. Depths are in meters below sea level

the atmosphere from 7.1 to 31.3 % with respect to the present anthropogenic CO₂ production of the Latium Region.

A 3D geological model (Fig. 2) of the selected structure was constructed on the basis of stratigraphical and reflection seismic data. Two main tectonic phases were likely responsible of the deep structural architecture of the area, which is characterized by isolated horst structures overlaid by caprock units, due to thrust-related folds offset by extensional faults

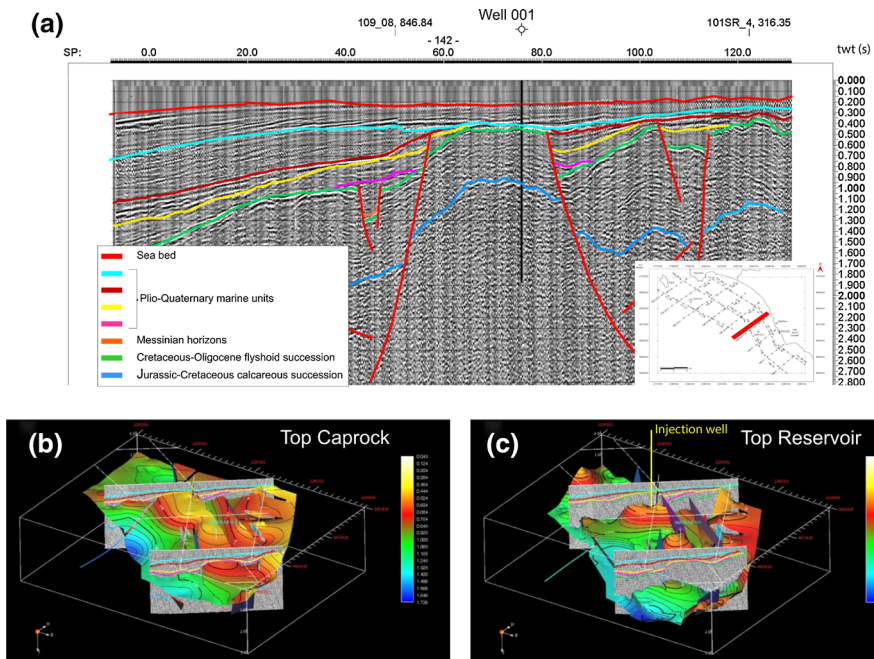


Fig. 2 The geological model construction included the re-interpretation of available seismic data (a) and the computation of structural maps of the main surfaces of top caprock (b) and top reservoir (b) units

(presently inactive). The geological model included tectonic discontinuities (e.g., normal faults) that likely represented the preferential pathways for CO₂ migration from the reservoir to the surface (Fig. 2a). Structural maps of the main surfaces of the top caprock and the top reservoir units were computed (Fig. 2b, c). A cross-correlation between the top reservoir units and seismic profiles was performed. A positive reservoir trap was identified and mapped (Fig. 2b).

The computed surfaces of the seismic horizons and faults were used to define a volumetric 3D model. The whole volume between such horizons was divided in 11 zones, and a potential injection well within the modeled structure was hypothesized (Fig. 1). Owing to the relatively wide dimensions of the model, two different simulations were performed at different scale: a simplified model consisting of 3D “column” centered in the injection well and a complex model with an area of 13.5 × 12.75 km and a vertical development of >3 km, including the portion of the selected structure between the two normal faults.

3 Modeling Approach

Numerical simulations were performed using the non-isothermal reactive geochemical transport code TOUGHREACT V1.2 (Xu and Pruess 2001; Xu et al. 2006) by means of the ECO2N model (Pruess 2005; Spycher and Pruess 2005), which allowed the description of the thermo-physical properties of mixtures of water and CO₂ at P-T conditions typically encountered in saline aquifers for CO₂ disposal (31 °C < T < 110 °C; 7.38 × 10⁶ Pa < P < 60.0 × 10⁶ Pa).

The code employs a sequential iterative approach to solve the coupling between transport and geochemical reactions. Flow and transport are based on space discretization by means of integral finite differences (Narasimhan and Witherspoon 1976). An implicit time-weighting scheme is used for the flow, transport, and kinetic geochemical equations. The chemical transport equations are solved independently for each component, while the reaction equations are worked out on a grid-block basis using the Newton–Raphson iteration.

Transport of aqueous and gaseous species by advection and molecular diffusion was considered in both liquid and gas phases. The diffusive contribution to the total mass of chemical species transported in liquid phase is governed by the following equation (Xu et al. 2004):

$$F_j = u_1 C_{jl} - (\tau \varphi S_1 D_1) \nabla C_{ji}, \quad (1)$$

where F is the mass flux ($\text{mol m}^{-2} \text{s}^{-1}$) of the aqueous chemical component j , u is the Darcy velocity (m s^{-1}), C is the concentration of the aqueous chemical component in the liquid phase (mol L^{-1}), τ is the tortuosity, φ is the porosity, S is the phase saturation, and D is the diffusion coefficient ($\text{m}^2 \text{s}^{-1}$).

Tortuosity was computed by TOUGHREACT according to Millington and Quirk (1961) equation:

$$\tau_\beta = \varphi^{1/3} S_\beta^{7/3}, \quad (2)$$

where S is phase saturation and β is phase index.

In our model, water density dependence on NaCl and CO₂ concentration (Garcia 2001) was taken into account by introducing some code adaptations to obtain more realistic simulations. The dependence of brine density on dissolved CO₂ was expressed according to the following equation (Garcia 2001):

$$\rho_{aq} = \rho_1 + M_2 c - c \rho_1 V_\varphi, \quad (3)$$

where V_φ is the apparent molar volume of dissolved CO₂; M_2 is the molecular weight of CO₂; ρ_1 is the density of pure water; and c is the concentration of CO₂ expressed by the number of moles of solute in 1 m³ of solution.

Further details on the process capabilities can be found in Xu and Pruess (2001) and Xu et al. (2006).

3.1 Geochemical Modeling

Geochemical calculations were performed under the local equilibrium assumption for aqueous complexation, acid-base, and gas dissolution/exsolution. Aqueous activity coefficients were computed using an extended Debye–Hückel equation by Helgeson et al. (1981). Fugacity coefficients of CO_{2(g)} were calculated by means of H₂O–CO₂ mutual solubility model of Spycher et al. (2005).

Mineral dissolution and precipitation proceeded under kinetic conditions for all the considered species (Table 1) according to the transition state theory (Lasaga 1984; Lasaga et al. 1994; Steefel and Lasaga 1994). A general equation, which includes temperature dependence of the rate constants and reaction terms for acid (H⁺), neutral and alkaline (OH⁻) mechanisms, was used for mineral dissolution (Lasaga et al. 1994; Palandri and Kharaka 2004; Marini 2007), as follows:

Table 1 Mineralogical phases considered for the simulations and thermodynamic parameters of the kinetic Eqs. (3–5)

Mineral	$k_{298,15}(\text{mol m}^{-2} \text{ s}^{-1})$			$E_a(\text{kJ mol}^{-1})$				
	Acid	Neutral	Base	Acid	Neutral	Base	n_1	n_3
<i>Primary mineral</i>								
K-feldspar	8.710×10^{-11}	3.890×10^{-13}	6.310×10^{-22}	51.7	38.0	–	0.50	0.823
Calcite	5.012×10^{-1}	1.549×10^{-6}	$3.311 \times 10^{-4*}$	14.4	23.5	35.4*	1.00	1.00*
Dol.-dis ^a	6.457×10^{-4}	2.951×10^{-8}	$7.762 \times 10^{-6*}$	36.1	52.2	34.8*	0.50	0.50*
Kaolinite ^a	4.898×10^{-12}	6.918×10^{-14}	8.913×10^{-18}	65.9	22.2	17.9	0.77	0.472
Quartz	–	5.888×10^{-13}	–	–	74.5	–	–	–
Illite	1.047×10^{-11}	1.660×10^{-13}	3.020×10^{-17}	23.6	35.0	58.9	0.34	0.40
Chlorite	7.762×10^{-12}	3.02×10^{-13}	–	88.0	88.0	–	0.5	–
Ca-Montm. ^a	1.950×10^{-13}	3.890×10^{-15}	3.890×10^{-15}	48.0	48.0	48.0	0.2	0.13
Muscovite	1.413×10^{-12}	2.818×10^{-14}	2.818×10^{-12}	22.0	22.0	22.0	0.37	0.22
Anhydrite	–	6.457×10^{-4}	–	–	14.3	–	–	–
Na-Smectite	1.047×10^{-11}	1.660×10^{-13}	3.020×10^{-17}	23.6	35.0	58.9	0.34	0.40
<i>Secondary mineral</i>								
Dawsonite	–	1.260×10^{-9}	–	–	62.8	–	–	–
Chalcedony	–	5.889×10^{-13}	–	–	74.5	–	–	–
Phlogopite	–	3.981×10^{-13}	–	–	29.0	–	–	–

Thermodynamic parameters are from Palandri and Kharaka (2004 and references therein). Rate constants are listed for dissolution. Dol.-dis: disordered dolomite. $k_{298,15}$ is the kinetic constant at 298.15 K. E_a is the activation energy and n is the order of the reaction (Eq. 4)

* Parameters for carbonate reactions depending on activity of $\text{CO}_{2\text{aq}}$

^a In some zones, this mineral is not initially present, but it can potentially precipitate as secondary mineral

$$r = S \left[\begin{array}{l} \left(k_{298,15\text{-acid}} \exp \left[\frac{-E_{a\text{-acid}}}{R} \left(\frac{1}{T} - \frac{1}{298.15} \right) \right] a_{\text{H}^+}^{n_1} \right) \\ + \left(k_{298,15\text{-neutral}} \exp \left[\frac{-E_{a\text{-neutral}}}{R} \left(\frac{1}{T} - \frac{1}{298.15} \right) \right] \right) \\ + \left(k_{298,15\text{-base}} \exp \left[\frac{-E_{a\text{-base}}}{R} \left(\frac{1}{T} - \frac{1}{298.15} \right) \right] a_{\text{OH}^-}^{n_3} \right) \end{array} \right] (1 - \Omega), \quad (4)$$

where r is the kinetic rate (positive values indicate dissolution, while negative values refer precipitation), S is the specific reactive surface area ($\text{m}^2 \text{ g}^{-1}$), $k_{298,15}$ is the rate constant at 298.15 K ($\text{mol m}^{-2} \text{ s}^{-1}$), E_a is the activation energy, R is the gas constant ($8.314 \text{ J mol}^{-1} \text{ K}^{-1}$), T is the absolute temperature (in Kelvin), a is the aqueous activity of the species, n is the order of the reaction, and Ω is the mineral saturation index. For carbonate reactions, catalyzed by HCO_3^- , the alkaline mechanism (a_{OH^-}) was substituted by the activity of aqueous $\text{CO}_2(a_{\text{CO}_2})$.

All the kinetic parameters reported in Eq. (4) are from Palandri and Kharaka (2004) and listed in Table 1. Kinetic illite data were set to those of smectite.

Specific reactive mineral surfaces are relatively difficult to be measured or calculated, especially for multi-mineral systems, since only selective sites of mineral surfaces participate to the reactions (e.g., Xu et al. 2007). Hence, during kinetic reactions, their areas may either increase or decrease as the mineral morphology changes (Wilson 1975; Grandstaff 1978; Berner and Holdren 1979; Berner and Schott 1982; Velbel 1984; 1986). This can result in

an uncertainty of the modeled results of up to several orders of magnitude (e.g., [Gautier et al. 2001](#)). In this study, reactive surface areas for each mineral (Table 2) were calculated as geometric surface area of a cubic array of truncated spheres ([Sonnenthal et al. 2005](#)) as observed by scanning electron microscopy analysis on the same rock samples outcropping inland ([Montegrossi et al. 2008](#)). For clay minerals, a plate-like grain was considered (e.g., [Marini 2007](#)). To account for both the surface roughness (discrepancy between the BET surface and the geometric areas; e.g., [White and Peterson 1990](#); [Zerai et al. 2006](#); [Marini 2007](#)) and the reaction of mineral surface selective sites ([Lasaga 1995](#); [Zerai et al. 2006](#)), reactive surface areas used in the numerical simulation were decreased by one order of magnitude (Table 2).

Precipitation of potential secondary minerals was represented with the same kinetic expression as for dissolution. Since kinetic parameters for precipitation rate are available for a relatively low number of minerals, only parameters for neutral mechanism were used to describe precipitation. Secondary minerals were assumed to have an initial surface reactive area equivalent to a truncated sphere with 2×10^{-6} m of radius, while a small volume fraction of 10^{-5} was assigned (Table 2).

The numerical simulation accuracy depends on the quality and consistency of the thermodynamic data. The primary source for equilibrium constants for aqueous species and minerals used in this study were generated with the EQ3/6 V7.2b database ([Wolery 1992](#)) and recalculated at reservoir pressure (20.4×10^6 Pa, computed in the centroid of the grid) by SUPCRT92 ([Johnson et al. 1992](#)) to ensure consistency with unmodified equilibrium constants.

4 Reconstruction of the Mineralogical and Petrophysical Properties of the Host-Aquifer and Cover Rocks: Data Input

Available site-specific information includes basic physical parameters such as temperature, pressure (following the hydrostatic gradient from sea bottom), and salinity (NaCl) of the formation waters (24 g L^{-1}). Therefore, the input data for numerical modeling of reactive transport simulations, such as mineralogical composition, petrophysical properties of the reservoir, and cover rocks (e.g., porosity and permeability), and chemical composition of formation waters (at reservoir conditions) prior of CO₂ injection were estimated. Bulk mineralogical composition and surface reactive area were obtained by analyzing the inland outcropping samples representative of the 11 zones recognized by the log data (Table 2).

The mineralogical composition was determined by combining calcimetric method (carried out with a Dietrich–Fruhling apparatus) and XRD Rietveld analysis after applying a correction for dolomite to the calcimetry determination. The Rietveld quantification procedure was performed by the diffraction/reflectivity analysis program Maud 2.2 ([Lutterotti et al. 1999](#)). Clay minerals were determined by XRD on the clay fraction ($<2 \mu\text{m}$) after the analysis of treated (oriented-, glycol- and 450 and 600 °C) samples.

The caprock is composed by allochthonous marly calcarenites and clay marls, which are made up of about 75 and 25 % (by vol.) by carbonate and silicate (quartz, smectite, muscovite, K-feldspar, and chlorite) minerals, respectively (Table 2). The hosting reservoir consists of pure limestone and marly limestone deposits with calcite and dolomite ranging from 60 to 90 % by total volume, respectively, and subordinate clay minerals (illite, chlorite, and Ca-montmorillonite) (Table 2). Triassic evaporites, mainly consisting of anhydrite and dolomite, represent the bottom of the sedimentary sequence.

Petrophysical properties such as porosity and permeability of rock formations were not available. Therefore, they were inferred by the well-log data and the mineralogical compo-

Table 2 Mineralogical composition and reactive area used in numerical simulations

Tectono-stratigraphical units		Caprock												
Mineral	Plio-quaternary marine units Zone 1		Cretaceous-oligocene flyshoid succession				Zone 4							
	Vol.	A	Vol.	A	Vol.	A	Vol.	A						
Calcite	21.9	584.4	92.2	285.9	68.3	14.3	81.3	428.9						
Quartz	6.0	597.7	3.0	1054.4	15.1	35.0	5.2	127.2						
Dol.-dis	1.2	557.6	0.0	376.9	1.7	13.7	0.0	409.2						
K-feldspar	5.3	621.1	–	–	–	–	–	–						
Na-smectite	15.9	659.9	–	–	–	–	–	–						
Illite	3.4	575.9	1.3	636.3	4.9	163.6	3.4	363.6						
Chlorite	5.2	597.7	0.1	618.4	1.9	137.4	3.1	353.4						
Kaolinite	2.1	604.5	0.0	443.6	–	408.6	0.0	408.6						
Muscovite	6.8	559.6	–	–	–	–	–	–						
Ca-Montm.	0.0	532.6	0.3	870.7	3.9	195.4	4.0	497.5						
Anhydrite	–	–	–	–	–	–	–	–						
Dawsonite	0.0	327.2	0.0	480.3	0.0	480.3	0.0	480.3						
Chalcedony	0.0	298.8	0.0	438.6	0.0	438.6	0.0	438.6						
Phlogopite	0.0	282.8	0.0	415.1	0.0	415.1	0.0	415.1						
Reservoir		Jurassic-cretaceous calcareous succession and upper triassic evaporites												
Mineral	Zone 5		Zone 6		Zone 7		Zone 8 ^a		Zone 9		Zone 10		Zone 11	
	Vol.	A	Vol.	A	Vol.	A	Vol.	A	Vol.	A	Vol.	A	Vol.	A
Calcite	58.1	395.0	90.5	316.0	59.5	1023.6	86.4	443.6	89.4	443.6	67.3	665.3	0.8	63.5
Quartz	34.2	684.6	3.1	75.2	28.3	68.0	3.3	33.7	0.5	33.7	0.5	61.9	–	–
Dol.-dis	0.0	376.9	0.0	377.0	0.0	317.4	0.0	317.4	0.0	317.4	21.6	976.8	0.2	60.6
K-feldspar	–	–	–	–	–	–	–	–	–	–	–	–	–	–
Na-smectite	–	–	–	–	–	–	–	–	–	–	–	–	–	–
Illite	1.0	162.2	1.1	778.5	0.2	655.7	–	–	–	–	–	–	–	–
Chlorite	0.2	157.6	–	–	0.2	637.1	–	–	–	–	–	–	–	–
Kaolinite	0.0	408.6	0.0	408.6	0.0	344.1	0.0	344.1	0.0	344.1	0.0	344.1	–	–
Muscovite	–	–	–	–	–	–	–	–	–	–	–	–	–	–
Ca-Montm.	1.3	221.9	0.0	455.5	1.8	897.1	0.2	897.1	–	–	0.5	992.9	–	–
Anhydrite	–	–	–	–	–	–	–	–	–	–	–	–	93.0	93.3
Dawsonite	0.0	442.3	0.0	372.5	0.0	372.5	0.0	372.5	0.0	372.5	0.0	372.5	0.0	426.3
Chalcedony	0.0	403.9	0.0	340.2	0.0	340.2	0.0	340.2	0.0	340.2	0.0	340.2	–	–
Phlogopite	0.0	382.3	0.0	322.0	0.0	322.0	0.0	322.0	0.0	322.0	0.0	322.0	–	–

Vol. abundance of minerals (% by total volume), *A* reactive area (cm²/g) calculated as geometric surface area of a cubic array of truncated spheres (Sonenthal et al. 2005). Volume of minerals refers to calculated composition after equilibrium simulation to reconstruct chemical composition of pristine formation water, *Dol.-dis* disordered dolomite, *Ca-Mont.* Ca-montmorillonite. For clay minerals, a plate-like grain was considered (e.g., Marini 2007). Concerning secondary minerals (dawsonite, chalcedony, and phlogopite), an initial reactive area equivalent to a truncated sphere with 2×10^{-6} m of radius was assumed

^a Marly facies of Zone 9, mineralogical composition was inferred by composition of Zone 9 (Morettini et al. 2002). A small volume fraction of 1×10^{-5} was assigned to secondary mineral in order to allow the surface area calculation

sition of the corresponding formations (Table 2) along with the use of boundary conditions such as superficial heat flow measurement and temperature profiles. A similar method was used by Singh et al. (2007).

The methodological approach was based on the relationships among thermal capacity, conductivity, porosity, and permeability to be established once the mineralogy of each formation (Montegrossi et al. 2008) was defined. The thermal properties were computed using a weighted sum of the thermal properties of each mineral, assigning an initial theoretic porosity of 1 % (Clauser and Huenges 1995; Singh et al. 2007). The model assumed that pores were filled with water whose thermal properties were sensibly different with respect to those of the minerals and that increasing the porosity, thermal capacity, and conductivity decreased. The limit of this procedure was assumption that it held only with Darcyan flow. This is true for permeability up to 10^{-12} m².

Consequently, the thermal properties were expressed as a function of porosity. Correlation models between porosity and permeability were well established, and they depended on the main mineralogical composition of each layer. On the basis of the mineralogical analysis, we used a clay-coating model for caprock, whereas for the reservoir rock, a calcite-coating model was considered. The coating model assumed the presence of small channel whose tortuosity and connectivity depended on the filling material (clay or calcite in our model), with a correction for the presence of quartz as vein filling material (e.g., Robertson 1988; Kuhn and Chiang 2003; Clauser 2006).

When a correlation model between porosity and permeability was established, in our system, the porosity was the only independent variable. For the calculation, we used the software SHEMAT (Kuhn and Chiang 2003) that also allows to compute the heat flow due to fluid advection. As boundary conditions, heat flow values from Cataldi et al. (1995) were considered. With a trial and error procedure, the best fit between our temperature and the well-log temperature profiles was computed, thus obtaining a porosity and permeability profile, whose results are reported in Table 3.

The chemical composition of pristine formation waters was unknown. Thus, for each zone, they were calculated by batch modeling (Table 4), assuming: (i) thermodynamic equilibrium among primary minerals (Table 2), (ii) NaCl (0.4 M) equivalent brines at specific temperature conditions (from 25 to 118 °C, Table 3), and (iii) pressure of 20.4×10^6 Pa. Batch modeling simulations were performed by PHREEQC V2.18 (Parkhurst and Appelo 1999), using the Lawrence Livermore National Laboratory database (lnl.dat), corrected by means of SUPCRT92 (Johnson et al. 1992) to match the average pressure (20.4×10^6 Pa) in the injection layer (zone 7). Database consistency with the EQ3/6 V7.2b database, used in TOUGHREACT, supported the use of the LLNL database. This approach was largely used to configure quantitative models of water–rock interactions (e.g., Gaus et al. 2005; Xu et al. 2005, 2010; Cantucci et al. 2009; Gundogan et al. 2011).

Possible secondary minerals, i.e., minerals that could precipitate when super-saturation conditions are achieved, were selected after batch modeling with PHREEQC, analyzing the saturation indexes of the available minerals derived by imposing kinetic reactions between the primary mineral assemblage and fluid (brine and CO₂) phases. Supersaturated minerals (i.e., dawsonite, kaolinite, and chalcidony), likely formed after CO₂ injection, were included in the model. Phlogopite was considered as the Mg end-member of clay mineral solid solutions following an ideal mixing (i.e. without mixing energy). For instance, the chemical composition of montmorillonite is formally equivalent to a simple mixing of a series of stoichiometric end-members (pyrophyllite, muscovite, talc, phlogopite; e.g. Fritz 1985). Consequently, only those end-members expected to be supersaturated were considered, without addressing the

Table 3 Petrophysical properties of the geological formations/zones used in the numerical simulations

Zone	P (Pa)	T (°C)	Density (kg m ⁻³)	Cond. T. (W/m °C)	Capac. T. (J/kg °C)	k _i (m ²)	φ _i	φ _c	n
<i>Caprock</i>									
1	2.4 × 10 ⁶	25	2400	2.08	1250	2.95 × 10 ⁻¹⁷	0.14	—	—
2	4.6 × 10 ⁶	32	2600	2.21	890	7.65 × 10 ⁻¹⁸	0.03	—	—
3	11.5 × 10 ⁶	55	2500	2.55	950	7.65 × 10 ⁻¹⁸	0.03	—	—
4	18.1 × 10 ⁶	76	2600	1.70	980	7.65 × 10 ⁻¹⁸	0.03	—	—
5	18.9 × 10 ⁶	79	2600	1.70	950	2.04 × 10 ⁻¹⁷	0.05	—	—
<i>Reservoir</i>									
6	19.3 × 10 ⁶	80	2600	2.13	970	2.04 × 10 ⁻¹⁷	0.05	0.046	4.974
7	20.4 × 10 ⁶	84	2600	2.13	1026	2.34 × 10 ⁻¹⁴	0.10	0.055	4.972
8	21.3 × 10 ⁶	87	2600	2.04	1040	1.02 × 10 ⁻¹⁵	0.10	0.044	4.975
9	23.2 × 10 ⁶	93	2600	2.04	1040	2.48 × 10 ⁻¹⁴	0.10	0.055	4.972
10	28.0 × 10 ⁶	108	2600	1.96	1072	2.48 × 10 ⁻¹⁴	0.10	0.055	4.972
11	30.8 × 10 ⁶	118	2800	4.08	920	1.84 × 10 ⁻¹⁶	0.06	0.043	4.824

Pressure (P) and temperature (T) are calculated in the centroid of each formation

Cond. T thermal conductivity, Capac. T thermal capacity, k_i initial permeability, φ_i initial porosity (Eqs. 5 and 6), φ_c critical porosity (Eq. 5), n power law exponent (Eq. 5)

resulting clay minerals whose behavior is rather unpredictable. Thus, for the sake of clarity, phlogopite was used throughout the text.

5 Problem Setup

The 3D geological model (Fig. 2) was used for the numerical models. Owing to the wide dimensions of the geological model, two different simulations were performed at different scale, starting from a geometrically simplified system. In the first model (“column”), the system was represented as a 3D vertical column centered on the injection well, whose dimensions were 0.11 × 0.11 × 3 km (8,470 elements). The grid was divided into 11 cells for the x and y axes and 70 cells for the z axis, according to the stratigraphic model of Fig. 1. The vertical resolution of the cells was from 9 to 120 m; a better refinement was carried out at the caprock–reservoir interface (Fig. 3). The injection was set in the center of the stratigraphic column (zone 7 in Figs. 1 and 3) at a rate of 1,500 t for 1 year due to the limited lateral dimensions of the model. The simulation was carried out for a time span of 100 years.

The second model (i.e., structure) was consisting of a 3D irregular grid with dimension of 13.5 × 12.75 × 3.8 km and covered the main portion of the structure enclosed between the recognized extensional faults. The grid included 150,470 elements with dimensions of approximately 250 m along the x and y axes, and a vertical resolution ranging from 15 to 300 m, with a major refinement at the caprock–reservoir interface and coarser cells in the upper and lower portions of the structure (Fig. 4). The hexahedral blocks followed the contact surfaces between the different horizons as derived by the seismic data. A vertical injection well was simulated in the upper part of the reservoir at the depth of 1,970 m (pink circle in Fig. 4). CO₂ was injected at the rate of 1.5 Mt year⁻¹ for 20 years. Owing to both the vast dimension of the structure and the long computation times, simulations were carried out for

Table 4 Chemical composition (mol/kg_w) of pristine formation waters at reservoir conditions, calculated assuming thermodynamic equilibrium between a NaCl equivalent brine (0.4 M) and minerals of each zone

Zone	pH	Ca ⁺²	Mg ⁺²	Na ⁺	K ⁺	Cl ⁻	HCO ₃ ⁻	SO ₄ ⁻²	Al ⁺³	SiO ₂	Fe ⁺²
1	7.83	6.38 × 10 ⁻⁴	1.20 × 10 ⁻³	0.368	2.64 × 10 ⁻⁵	0.368	2.98 × 10 ⁻³	9.86 × 10 ⁻⁷	6.74 × 10 ⁻⁷	9.11 × 10 ⁻⁵	4.42 × 10 ⁻¹⁰
2	7.77	3.72 × 10 ⁻⁴	3.20 × 10 ⁻³	0.376	1.86 × 10 ⁻²	0.393	9.11 × 10 ⁻³	9.87 × 10 ⁻⁷	5.78 × 10 ⁻⁷	1.24 × 10 ⁻⁴	9.87 × 10 ⁻¹³
3	7.63	1.81 × 10 ⁻³	1.59 × 10 ⁻³	0.363	2.51 × 10 ⁻²	0.392	2.68 × 10 ⁻³	9.89 × 10 ⁻⁷	1.26 × 10 ⁻⁷	2.82 × 10 ⁻⁴	9.89 × 10 ⁻¹¹
4	7.64	2.58 × 10 ⁻⁴	4.25 × 10 ⁻⁵	0.376	2.36 × 10 ⁻²	0.395	4.77 × 10 ⁻³	1.00 × 10 ⁻⁶	3.52 × 10 ⁻⁶	5.05 × 10 ⁻⁴	1.00 × 10 ⁻¹⁰
5	7.75	2.41 × 10 ⁻⁴	3.13 × 10 ⁻⁵	0.375	2.36 × 10 ⁻²	0.394	5.33 × 10 ⁻³	1.00 × 10 ⁻⁶	3.28 × 10 ⁻⁶	5.57 × 10 ⁻⁴	1.00 × 10 ⁻¹⁰
6	7.63	2.34 × 10 ⁻⁴	3.07 × 10 ⁻⁵	0.376	2.37 × 10 ⁻²	0.395	4.72 × 10 ⁻³	1.00 × 10 ⁻⁶	3.29 × 10 ⁻⁶	5.43 × 10 ⁻⁴	1.00 × 10 ⁻¹⁰
7	7.59	2.36 × 10 ⁻⁴	1.85 × 10 ⁻³	0.378	2.03 × 10 ⁻²	0.396	1.22 × 10 ⁻²	1.00 × 10 ⁻⁶	2.67 × 10 ⁻⁶	5.64 × 10 ⁻⁴	1.00 × 10 ⁻¹⁰
8	7.62	8.10 × 10 ⁻⁴	2.97 × 10 ⁻³	0.379	4.11 × 10 ⁻²	0.396	1.56 × 10 ⁻²	1.00 × 10 ⁻⁶	7.80 × 10 ⁻⁶	6.10 × 10 ⁻⁴	1.00 × 10 ⁻¹⁰
9	7.54	3.66 × 10 ⁻³	7.60 × 10 ⁻¹⁰	0.394	1.00 × 10 ⁻⁶	0.395	7.02 × 10 ⁻³	1.00 × 10 ⁻⁶	4.70 × 10 ⁻⁶	6.57 × 10 ⁻⁴	1.00 × 10 ⁻¹⁰
10	7.53	2.40 × 10 ⁻³	7.15 × 10 ⁻⁴	0.393	1.00 × 10 ⁻⁶	0.393	5.88 × 10 ⁻³	1.00 × 10 ⁻⁶	1.67 × 10 ⁻⁶	9.97 × 10 ⁻⁴	1.00 × 10 ⁻¹⁰
11	7.41	7.88 × 10 ⁻³	2.14 × 10 ⁻³	0.392	1.00 × 10 ⁻⁶	0.391	2.49 × 10 ⁻³	9.64 × 10 ⁻³	1.00 × 10 ⁻³	9.87 × 10 ⁻⁶	1.00 × 10 ⁻¹⁰

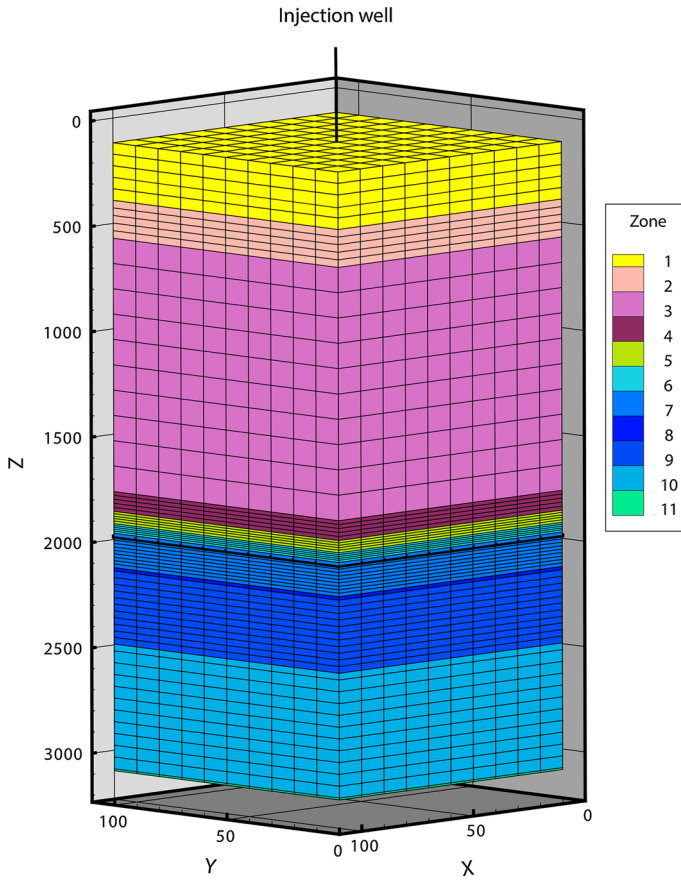


Fig. 3 Mesh 3D of the column model. The **bold black line** indicates the layer target of the injection (zone 7). Values of z are referred to the stratigraphic column of Fig. 1

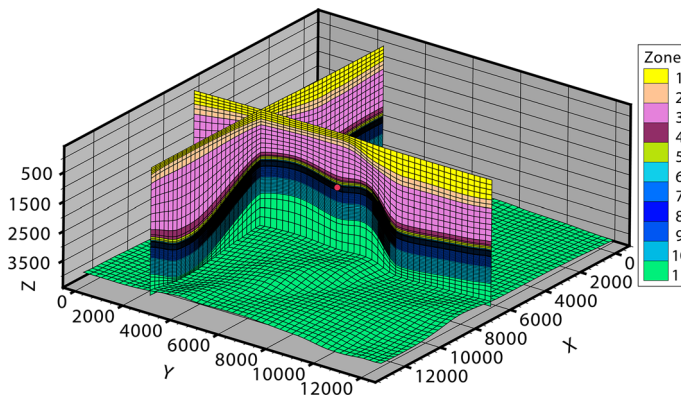


Fig. 4 3D mesh of the structure model. The *pink circle* is the injection point. Values of z are referred to the stratigraphic column of Fig. 1

Table 5 Hydrogeologic parameters and equations used for numerical simulations

Relative permeability (Corey 1954)	
Liquid	Gas
$k_{rl} = \hat{S}^4$	$K_{rg} = (1 - \hat{S})^2 (1 - \hat{S}^2)$
$\hat{S} = (S_l - S_{lr}) / (1 - S_{lr} - S_{gr})$	S _{gr} (irreducible gas saturation) = 0.05
Sl: liquid saturation	
S _{lr} (irreducible water saturation) = 0.1	
Capillary pressure (Milly 1982)	
$P_{cap} = -97.783 \times 10^4$	$A = 2.26 \left(\frac{0.371}{S_l - S_{lr}} - 1 \right)^{1/4}$
Sl: liquid saturation	
S _{lr} (irreducible water saturation) = 0.1	

a time span of 40 years. The relatively short time can partly be justified by the high reaction rates of carbonate minerals hosting the selected reservoir.

In both models, the 11 stratigraphic units, from the sea floor to the reservoir bottom (Fig. 1), were included in order to be consistent with both the lithological and stratigraphical features identified in the geological model. For both simulations, the same boundary conditions, listed in Tables 1, 2, 3, and 4, were used. The system was assumed as a porous medium, fully saturated with a NaCl 0.4 M brine, with homogeneous properties within each zone (conceptual layers).

Due to the presence of two extensional faults, horizontally delimiting the reservoir (Fig. 2), the system can be considered closed with a constant pressure out-flux at the reservoir bottom (zone 10), which represents the regional hydrostatic flux boundary. No flux conditions were set for the other boundaries of the domain.

The injection of CO₂ was simulated to occur at the depth of 1,970 m (Fig. 1) at hydrostatic pressure and temperature of the injection cell (about 81 °C, Table 3). According to the boundary conditions, the computational domain of the structure model was calibrated to include laterally the whole structure and vertically the thermal constrain of the sea floor (i.e., 17 °C) and the lower layer of the structure (zone 11; 118 °C). The vertical meshing was only refined in the caprock–reservoir layers, and the resolution of the structure model was limited for numerical reasons. The result was a relatively coarse mesh, which can introduce a not negligible numerical diffusion, thus leading to an overestimation of the dissolved CO₂ in the brine. However, the comparison with a finer grid (like in the column model) allowed to evaluate the extent of this approximation, without losing the focus on the general reservoir behavior.

It should also be highlighted that this grid distribution did not permit to represent the buoyant forces in detail, where CO₂-rich waters were migrating downward favoring the vertical brine-CO₂ mixing (Weir et al. 1995; Garcia 2001). The representation of these processes would require a much finer grid than those used in this work, a resolution that is problematic for large-scale models. Moreover, significant vertical mixing generally occurs on a time scale of hundreds to thousands of years (e.g., Ennis-King and Paterson 2003; Xu et al. 2007), and it can approximately be comparable to time scales for significant geochemical interactions of CO₂. Nevertheless, diffusion was taken into account because the diffusive fluxes could greatly be enhanced by chemical reactions due to the concentration gradient resulting from any reaction front.

Formulation for relative permeability (k_{rl} and k_{rg}) was from Corey (1954), whereas the capillary pressure followed the Milly's equation (Milly 1982), with a liquid and gas irreducible

saturation of 0.1 and 0.05, respectively (Table 5). The diffusion coefficients of CO₂ within the liquid phase and of water within the gas phase (CO₂) were computed from fluid viscosity (Palmer 1994; Frank et al. 1996; Wang et al. 1996; Hashimoto and Suzuki 2002; Tamini et al. 1994) at average reservoir conditions, and set at $4.04 \times 10^{-9} \text{m}^2 \text{s}^{-1}$ and $1.59 \times 10^{-3} \text{m}^2 \text{s}^{-1}$, respectively. These values were employed for each formation considered in the model.

Mineral dissolution and precipitation reactions involved temporal changes in reservoir porosity and permeability, modifying fluid flow and transport of CO₂. To account for this phenomenon, in our model, a feedback between fluid flow and geochemical reactions was considered with an increase of the computational time.

Several models describing the porosity–permeability relationship are available in the TOUGHREACT code. In the present paper, permeability changes were evaluated using the porosity–permeability relationship model of Verma and Pruess (1988) for the reservoir (Eq. 5) and the cubic law model (Steefel and Lasaga 1994) for the caprock (Eq. 6);

$$\frac{k}{k_i} = \left(\frac{\varphi - \varphi_c}{\varphi_i - \varphi_c} \right)^n, \quad (5)$$

$$k = k_i \left(\frac{\varphi}{\varphi_i} \right)^3, \quad (6)$$

where k is the modified permeability, k_i and φ_i are the initial permeability and porosity, respectively, φ_c is critical porosity value at which permeability is zero, and n is the power law exponent; φ_c and n are medium-dependent (see below). Parameters for Eqs. (5) and (6) are reported in Table 3.

Because of the complexity and diversity of the pore geometry of natural geologic media, a generally valid porosity–permeability relationship is not always valid for all porous media (Raffensperger 1996), and in some cases different formulations may be preferable (Pape et al. 1999; Xu et al. 2004).

The choice to apply two different porosity–permeability relationships for caprock and reservoir is due to the availability of experimental data of reservoir formations, belonging to Jurassic-Cretaceous calcareous successions. For these successions, some porosity–permeability values are reported in the scientific literature (e.g., Agosta et al. 2007) and in the hydraulic test of some well logs (<http://www.vidempi.com>). Equation (5), used for the reservoir, was fitted with the available porosity–permeability values to obtain critical porosity values and power law exponent (Table 3). For the caprock successions, characterized by Cretaceous-Oligocene Flyshoid succession, no data were available. Then, a simpler equation such as the cubic law (Eq. 6) was preferred. This relationship accurately describes the flow through the fractures and is used in several carbonatic systems (e.g., Witherspoon et al. 1980, 2010; André et al. 2007) and fluid–rock reactions (e.g., Yasuhara et al. 2006). The cubic law is very sensitive to small variation of porosity and is relatively simple to be handled especially when an experimental constrain of the porosity–permeability correlation is not directly available.

6 Preliminary Modeling Results

6.1 The Column Model

6.1.1 The Column Flow-Only Model

The CO₂ injection in the column model was firstly evaluated from a hydrodynamic point of view, i.e., neglecting geochemical reactions.

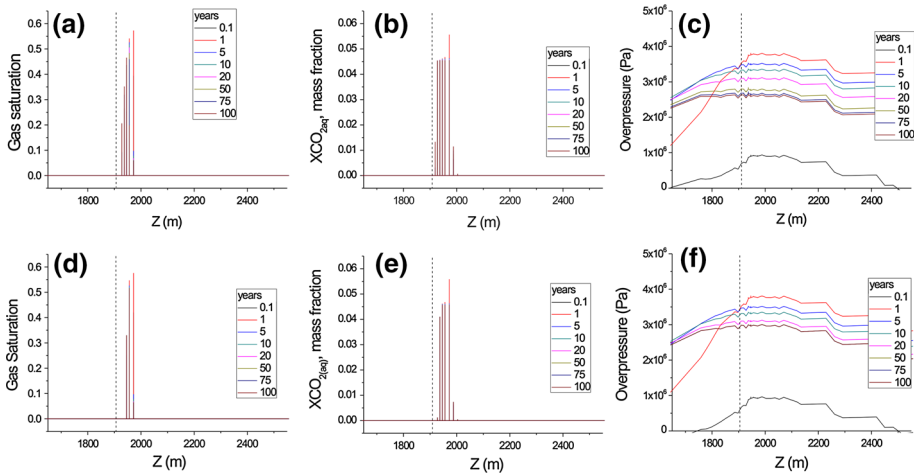


Fig. 5 Temporal evolution versus z of **a** gas saturation, **b** aqueous CO₂ fraction (XCO_{2aq}), **c** overpressure (Pa) in the column flow-only model, **d** gas saturation, **e** aqueous CO₂ fraction (XCO_{2aq}), **f** overpressure (Pa) in the column reactive flow model. Values of z are referred to the stratigraphic column of Fig. 1

Figure 5a shows the CO₂ plume extension over the time. At the end of the injection, the upper layers of zone 7 are partially saturated in CO₂ (gas saturation of 0.57). In this area, a two-phase zone containing both aqueous solution and supercritical CO₂ exists. The width of the CO₂ plume and the saturation profile across the model are strictly associated with the injection rate, the permeability, and the relative permeability of the system.

After 20 years from the injection, gas saturation (SG) slowly decreases to 0.06 in the injection cell, while the CO₂ plume moves upward due to buoyancy forces. At the end of the simulations (i.e., 100 years), the two-phase zone extends up to the central part of zone 6.

The fraction of dissolved CO₂ (XCO_{2aq} ; Fig. 5b) achieves the maximum value of 0.055 mass fraction in the injection cell after 1 year; according to the pressure distribution, it reaches the intermiddle parts of zone 6 (0.001 aqueous CO₂ mass fraction) and 7. After 100 years, the XCO_{2aq} maximum value is about 0.045 in the upper part of the reservoir. Apart those elements in contact with the CO₂ plume, small amount of CO_{2(aq)} can be observed in the cells below the injection layer up to 20 m downward. The overpressure of the system, calculated as the difference between the pressure at 1, 5, 10, 20, 50, 75, and 100 years and that before the injection, shows a maximum value of 3.7×10^6 Pa at the end of the injection in a large part of the reservoir and completely affects zones 7 and 6. As the injection ends, the overpressure gradually decreases to $\sim 3.1 \times 10^6$ Pa after 20 years (Fig. 5c) and $\sim 2.6 \times 10^6$ Pa after 100 years.

6.1.2 The Column Reactive Flow Model

When geochemical reactions are coupled with the hydrodynamic features, significant variations in the CO₂ behavior are recognized. In particular, after 20 years, CO₂ dissolution and porosity–permeability feedback, derived from minerals reactions, limit the CO₂ plume extent from the injection cell to the lower layer of zone 6 (gas saturation of 0.31; Fig. 5d), with respect to the flow-only model, whose effects were observed in the middle part of zone 6 (Fig. 5a). Similarly, the distribution of XCO_{2aq} also varies. After 20 years from the injection, XCO_{2aq} is indeed lower (0.029; Fig 5e) in the reactive flow simulation than that obtained in

the flow-only run (0.045; Fig 5b), likely due to the pH lowering computed by the chemical reactions. At the end of the simulations, $\text{XCO}_{2\text{aq}}$ affects the middle part of zone 6, in contrast with the flow-only model, where only the upper part of the reservoir was interested.

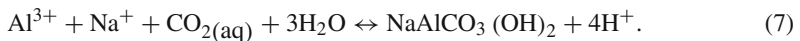
On the other hand, little differences in the overpressure distribution are observed (Fig. 5f) mainly due to the relatively small amount of CO_2 consumed by the chemical reactions. The overpressure behavior is consistent with those of the flow-only model up to 50 years of simulation; then the overpressure stabilizes at 3.0×10^6 Pa up to the end of the run, likely due to the formation of secondary minerals, which reduces the plume distribution.

As CO_2 enters the reservoir, the system under investigation is characterized by strong reactivity mainly centered in the injection zone. In the injection cell, the dissolution of CO_2 produces a sharp variation of pH that decreases from 7.6 to 4.8 (Fig. 6a) in a few months. This favors carbonate (i.e., calcite) dissolution that partially buffers the system. Due to the fast kinetics of calcite, pH slightly increases, and it tends to stabilize at a value of nearly 5 until the end of simulation period. The relatively high concentration of H^+ allows the dissolution of about -0.02 % by vol. of calcite from the initial value in the injection cell in the first year and of -0.13 % by vol. (Fig. 6b) after 100 years. Chlorite (-0.07 % by vol.) and Ca-montmorillonite (-0.012 % by vol.) dissolve, though at relatively low extent, causing an increase in porosity and permeability ($+0.14$ % by vol. and $+3.9 \times 10^{-15}$ m^2 , respectively; Fig. 6d, e, k, l). The amount of dissolved CO_2 in the aqueous phase at the end of the injection is 1.3 mol kg^{-1} , which decreases down to 1 mol kg^{-1} in the injection cell after 100 years, due to mineral trapping. At the end of the simulation, a maximum concentration of 1.1 mol kg^{-1} is achieved at the bottom of zone 6 (Fig. 7a).

From the injection cell, CO_2 slowly rises up to the bottom of zone 6 due to buoyancy forces. In this layer, the CO_2 impact is more evident. The values of pH show a significant decrease (from 7.59 to 4.8) within 1 year, reaching a value of 5 after 100 years. The presence of CO_2 produces the dissolution of calcite (up to -0.23 %), chlorite (-0.07 % by vol.), Ca-montmorillonite (-0.012 % by vol.) and, at minor extent, quartz (-1×10^{-3} % by vol.), favoring the increase of porosity ($+0.23$ %) and permeability ($+6.5 \times 10^{-15}$ m^2) (Fig. 6).

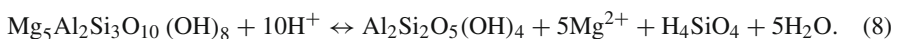
After few years from the end of the injection, the high concentrations of Ca^{2+} and HCO_3^- allow the re-precipitation of secondary calcite in the zone 6 of $+0.02$ % by vol. and $+0.58$ % by vol. after 100 years.

Kinetic simulations suggest that dissolution of carbonate and Al-silicate (i.e., chlorite and Ca-montmorillonite) minerals, catalyzed by high concentrations of Na^+ , favors the precipitation of dawsonite (Fig. 6i) in the upper part of zone 7 after 10 years (up to 0.0025 % by vol.), thus trapping part of injected CO_2 , as follows:



At 20 years, dawsonite partially dissolves (-0.0013 % by vol.), and after 50 years, it is completely consumed.

Chlorite, dissolving in the injection zone, starts to re-precipitate (as observed by Balashov et al. 2013) after 10 years of injection, reaching values of $+0.006$ % by vol. in the injection zone 7 after 100 years. The released of Mg^{2+} from chlorite dissolution is partly allocated in both disordered dolomite (0.006 % by vol.) and phlogopite-like mica (0.001 % by vol.) after 10 and 50 years, respectively (Fig. 6h, j). The incongruent dissolution of silicate minerals produces the precipitation of illite ($+0.006$ and $+0.05$ % by vol. after 5 and 100 years, respectively) and kaolinite ($+0.001$ and $+0.0013$ % by vol. after 20 and 100 years, respectively), the latter being a secondary mineral, which forms according to the following reaction:



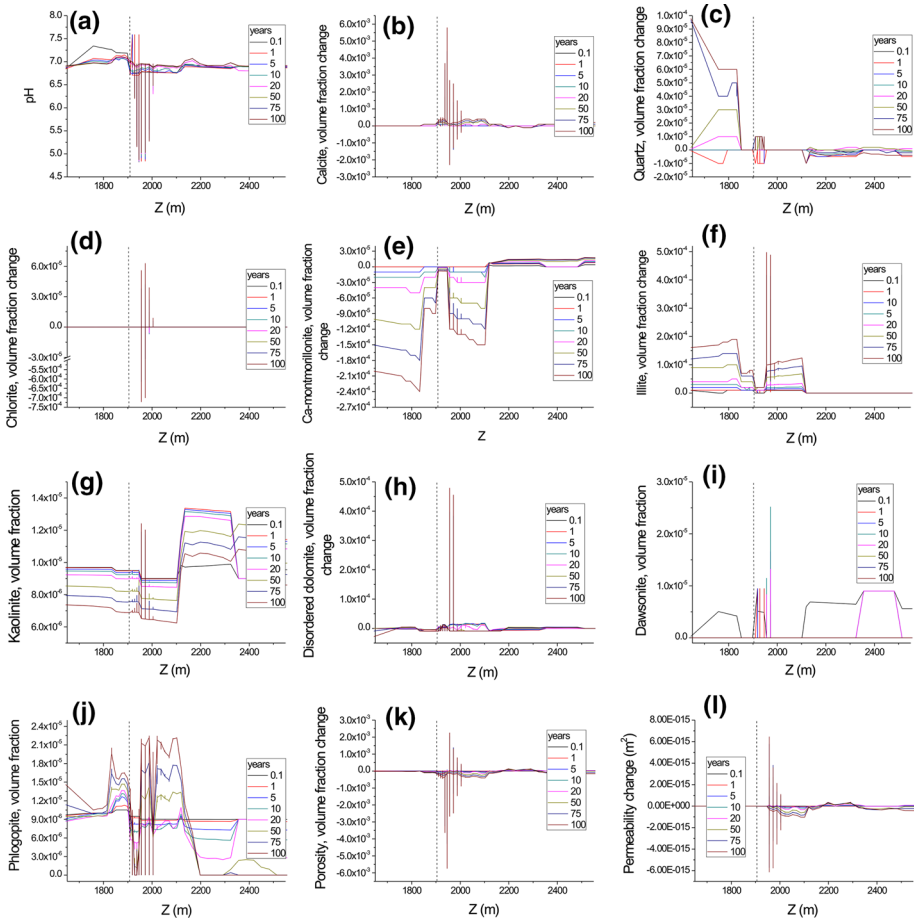


Fig. 6 Temporal evolution versus z of **a** pH, **b** delta calcite, **c** delta quartz, **d** delta chlorite, **e** delta Ca-montmorillonite, **f** delta illite, **g** kaolinite (fraction volume), **h** delta disordered dolomite, **i** dawsonite (fraction volume), **j** phlogopite (fraction volume), **k** delta porosity, and **l** delta permeability (m^2) in the column reactive flow model. Deltas refer to the volume fraction changes. Values of z are referred to the stratigraphic column of Fig. 1

On the other hand, a fluid rich in salt and less acidic ($pH = 5.2$) moves into the lower layers of zone 7, only slightly affecting water chemistry. Calcite slightly dissolves (up to -0.08% by vol.) along with Ca-montmorillonite (-0.014% by vol.), while illite ($+0.012\%$ by vol.) and displaced calcite (up to 0.15% by vol.) precipitate (Fig. 6b).

Among secondary minerals, only disordered dolomite (0.048% by vol.) and phlogopite ($+0.002\%$ by vol.) form after 100 years. Quartz and chlorite content remained unchanged.

At the end of the simulation, the CO₂-rich fluid affects the upper layers of the reservoir (zones 7 and 6), as showed by the pH values, which range between 5 and 6 (Fig. 6a). In the remaining sector of the reservoir (zones 8–10), some variations in the mineral behavior are recognized (Fig. 6), although the pH values, ranging from 6.5 to 7, suggest that these differences are mainly due to water–rock interaction processes rather than to reactions induced by the presence of CO₂.

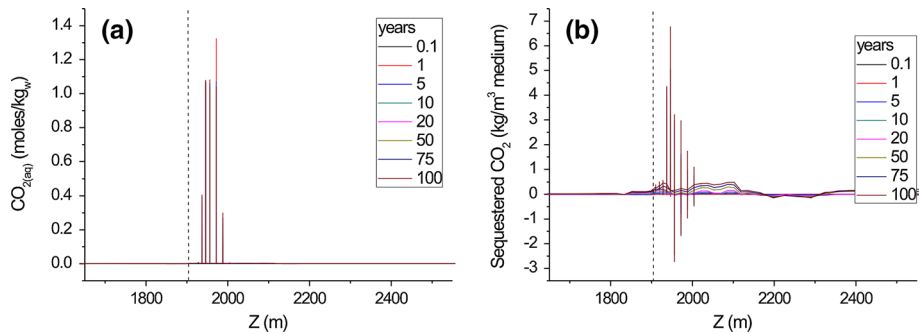


Fig. 7 Temporal evolution versus z of **a** $\text{CO}_{2(\text{aq})}$ (moles/kgw) and **b** sequestered CO_2 ($\text{kg}/\text{m}^3 \text{CO}_2$ of medium) in the column reactive flow model. Values of z are referred to the stratigraphic column of Fig. 1

Calcite and secondary carbonates control the sequestered CO_2 as mineral trapping (here defined as the difference between dissolved and precipitated carbonates). The sequestered CO_2 is negative in the injection cell ($-1.67 \text{ kg}/\text{m}^3$ of medium), in the underlying strata ($-0.95 \text{ kg}/\text{m}^3$ of medium), and in the upper cells of zone 7 ($-2.7 \text{ kg}/\text{m}^3$ of medium). Vice versa, significantly positive values are recorded in the zone 6 (up to $6.8 \text{ kg}/\text{m}^3$ of medium) after 100 years (Fig. 7b). Minerals dissolution and precipitation regulate the porosity and permeability evolution. Porosity follows calcite and mineral trapping trend, decreasing in the zone 6 from 5 to 4.4 % (up to -0.6% by vol.). Permeability follows the same tendency, decreasing from 2.34×10^{-14} to $1.74 \times 10^{-14} \text{ m}^2$ in the zone 7. The influence of the precipitation of non-carbonate minerals on porosity and permeability variation can be considered negligible.

The analysis of the caprock–reservoir interface (Fig. 6) shows that the CO_2 plume is retained into the zone 6. The calculated pH values in the bottom of the zone 5 (caprock) and in the upper layer of the zone 6 (reservoir) are indeed around 7. Moreover, after 100 years, small amounts of secondary calcite ($+0.016$ by vol.), phlogopite ($+0.0001 \%$ by vol.), and illite ($+0.008 \%$ by vol.) are observed in correspondence of the caprock–reservoir interface. Porosity decreases of -0.01% by vol. leading to a further sealing of reservoir.

Intermiddle results between the flow-only and the reactive flow models are observed when considering a simulation that only includes the calcite contribution to the geochemical reactions (calcite model). The hydrodynamic variables of calcite model (i.e., SG, overpressure and $\text{XCO}_{2\text{aq}}$) follow the flow-only model distribution, overestimating the plume extent (up to the central part of zone 6) with respect to the column reactive model (the lower layer of zone 6; Fig. 8). After 100 years, the central part of zone 6 is partially saturated in CO_2 , although the SG value is lower than that in the flow-only model (0.11 vs. 0.20) due to CO_2 dissolution and calcite reaction (Fig. 8a). A similar behavior is shown by $\text{XCO}_{2\text{aq}}$ (not shown), since in the central part of zone 6, its value is of 0.004. Overpressure (not shown) mimics the flow-only model with a maximum value of $3.7 \times 10^6 \text{ Pa}$ at the end of the injection. The impact on the chemical system is also evidenced when comparing the resulting pH distribution (Fig. 8b), which is one of the key variables of the system, and it better reflects the effect of a complex mineralogical composition with respect to the calcite model. Differently from the reactive flow model, the pH distribution shows that part of the injected CO_2 affects the lower layer of the caprock. The pH values change from the initial value 7.75 to 6.31 after 100 years. Calcite (not shown), after an initial dissolution in the injection zone, starts to re-precipitate after 20 years (up to 0.01 % by vol. after 100 years), but contrarily to the reactive flow model, no self-sealing phenomena are observed at the caprock–reservoir interface. Both porosity and

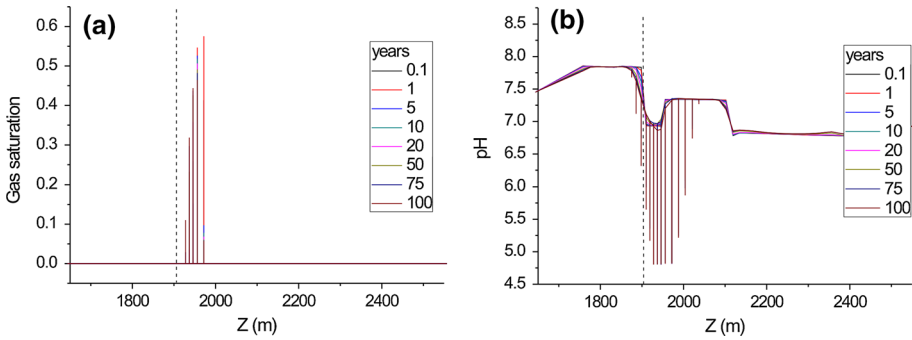


Fig. 8 Temporal evolution versus *z* of **a** gas saturation and **b** pH in the column calcite model. Values of *z* are referred to the stratigraphic column of Fig. 1

permeability (not shown) decrease due to calcite precipitation, even though at a minor extent (−0.12 % by vol. and $-3.14 \times 10^{-15} \text{ m}^2$, respectively, after 100 years) with respect to the reactive flow model. Although calcite reaction is the main process in the column model, the results of the calcite model highlight the sensitivity of the system to the geochemical and mineralogical composition.

6.2 The Structure Model

The investigation of the geochemical reactions and the CO₂ flow through the entire structure allowed to: (i) study the distribution of the CO₂ plume, (ii) quantify the entity of the mineral trapping mechanism, and (iii) verify the porosity and permeability changes induced by fluid–rock interaction and injectivity. The comparison with the results obtained by the column model also permitted to evaluate the effects of the grid scaling on the chemical reactions and the introduction of a complex geometry, the latter affecting the CO₂ plume migration over time.

6.2.1 The Structure Flow-Only Model

The hydrodynamic results obtained from the CO₂ injection in the structure at 20 (end of injection) and 40 years are shown in Fig. 9. During the injection phase, the CO₂ plume driven by buoyancy forces moves upwards from the injection cell, reaching the two structural highs of the reservoir. After 20 years, the plume evolves vertically from the lower part of zone 6 to the upper part of zone 9 (about 200 m) and covers an area of 3.5 km in diameter (Fig. 9a). The maximum gas saturation value in the injection cell is 0.88. At the end of the simulated run (i.e., 40 years), the bi-phase zone, containing both aqueous solution and supercritical CO₂, spreads out horizontally up to 3.75 km diameter, reducing its thickness to 75 m. The maximum gas saturation values of ~0.7 can be found in correspondence of the structural highs of the structure (Fig. 9b). The injection of CO₂ in a relatively low permeability reservoir produces an overpressure of $4 \times 10^6 \text{ Pa}$ in a large part of the reservoir after 20 years, and a maximum value of $4.8 \times 10^6 \text{ Pa}$ is achieved in the injection zone. A general increase of pressure (from 2.0 to $3.0 \times 10^6 \text{ Pa}$ of overpressure) is generally recorded in whole structure (Fig. 9c). When the injection ends, the simulated overpressure is as high as $3.6 \times 10^6 \text{ Pa}$ in both the entire reservoir and the lower part of the caprock (Fig. 9d).

Pressure controls the fraction of dissolved CO₂ (Fig. 9e, f). As the injection ends, the gas saturation decreases, and the aqueous CO₂ fraction slightly increases due to CO₂ dissolution

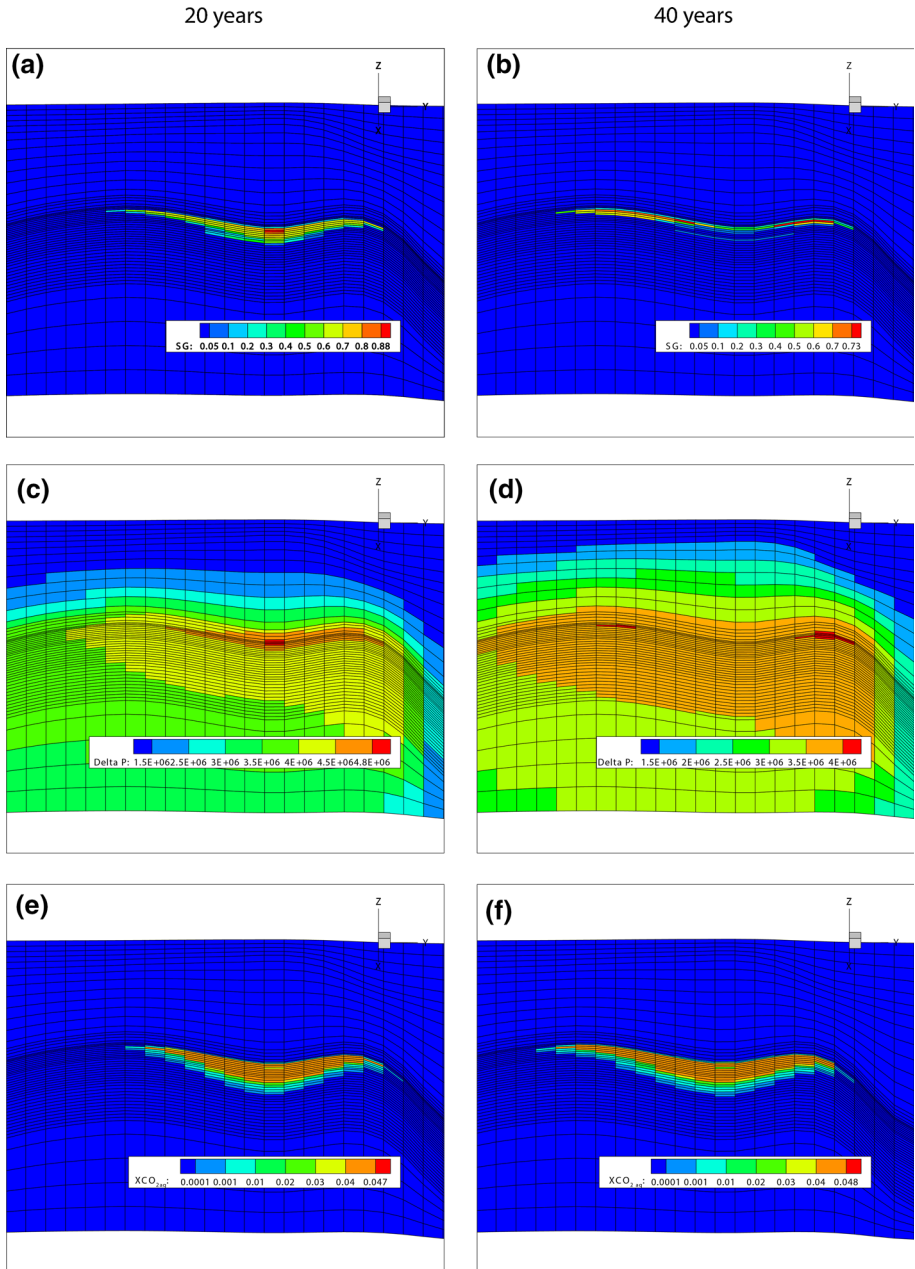


Fig. 9 Spatial distribution (zoomed in the reservoir) of gas saturation (SG) at 20 (a) and 40 years (b), overpressure (Pa) at 20 (c) and 40 years (d); aqueous CO_2 fraction ($X_{\text{CO}_2\text{aq}}$) at 20 (e) and 40 years (f) into the structure flow-only model. Injection was simulated for 20 years. Close to the injection point grid spacing is 250 m along the x - y axes and 15 m along the z axis

in the formation waters (0.048 after 40 years). The CO_2 -rich waters move downward driven by density differences and diffusive processes. The downward movement is 400 m and 430 m after 20 and 40 years, respectively. It should be noted that the fluid flow of the water displaced

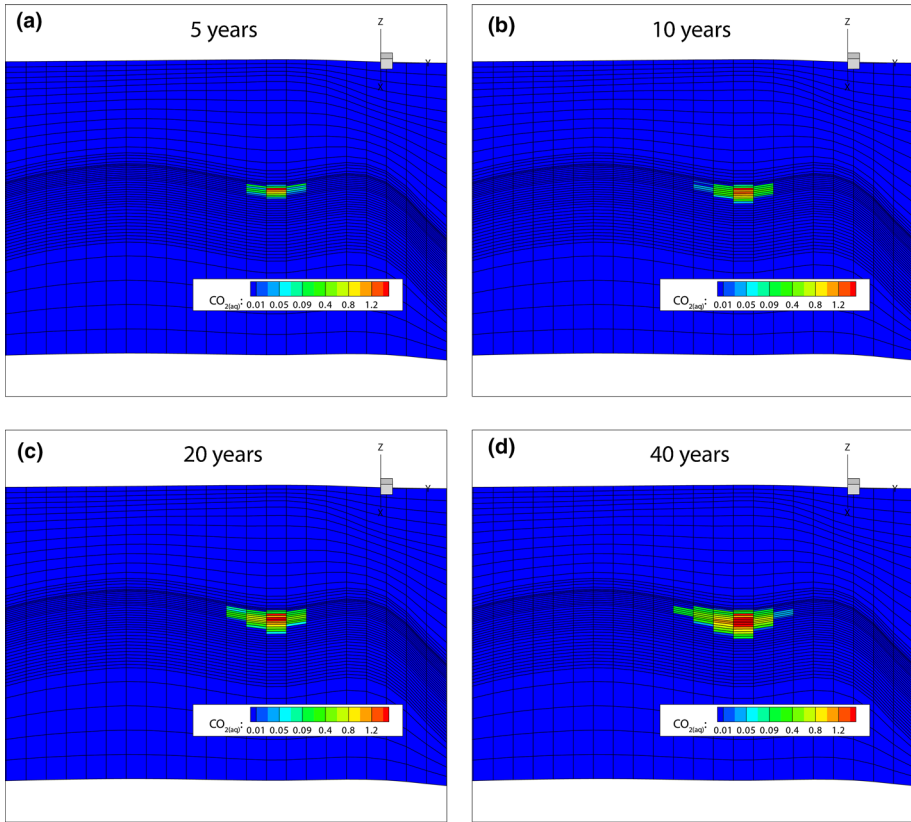


Fig. 10 Spatial distribution of aqueous CO_{2(aq)} in the structure reactive flow model after 5 (a), 10 (b), 20 (c), and 40 (d) years of simulation. Injection was simulated for 20 years. Grid spacing as in Fig. 9

by the CO₂ injection in the first 20 years and by the successive plume relaxation superimposes to the mentioned effect. These processes also affect any expected upward branches of the convective cell, although they are not observed likely because jeopardized by such downward fluid flow directed toward the constant pressure boundary.

6.2.2 The Structure Reactive Flow Model

The evolution of CO_{2(aq)} over the time is highlighted in Fig. 10. In the first 40 years of simulation, CO₂ distribution in the structure is affected by dissolution (solubility trapping) and chemical reactions (mineral trapping). After 5 years (Fig. 10a), CO_{2(aq)} extends vertically for 204 m, occupying the central area of the structure from the lowermost part of zone 6 to zone 8. After 10 years (Fig. 10b), the plume is in the upper part of zone 9, and after 20 years of injection, it extends for an area of 1,000 m in diameter with a vertical development of 300 m. As the plume broadens due to overpressure relaxation, it reaches a maximum extent of about 1,350 m along the x and y axes and 420 m in the z axis (Fig. 10d). After 40 years, the caprock is not affected by the injection of CO₂.

The evolution of pH (Fig. 11) mimics the behavior of the CO_{2(aq)} plume. A relatively acidic CO₂-rich fluid expands horizontally from the injection zone (pH = 4.7) following the morphology of the structure. After 40 years, the CO₂-rich water with pH = 5.9 reaches the

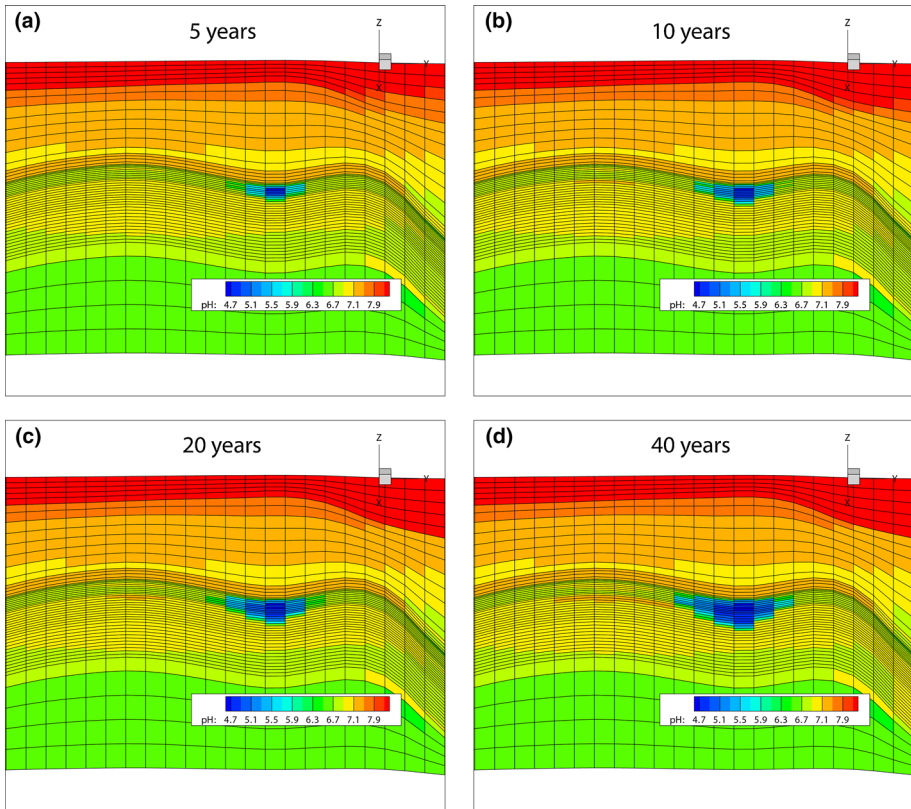


Fig. 11 Spatial distribution of pH after 5 (a), 10 (b), 20 (c), and 40 (d) years of simulation in the structure reactive flow model. Pre-injection pH values are reported in Table 4. Grid spacing as in Fig. 9

intermeddled layers of the zones 6 and 9, with a lateral extent of about 1,350 m (Fig. 11d). Around and above the acidic fluid, a zone with neutral pH (6.9) occurs. According to the column simulation, the most important process controlling the mineral trapping, and the injectivity is the dissolution/precipitation of calcite and, at minor extent, dolomite.

Calcite (expressed as volume fraction change) varies with time as shown in Fig. 12. In the first 5 years of simulation (Fig. 12a), calcite dissolves of -0.03% by vol. in the injection cell and in the closest elements, where pH is as low as 4.7 (Fig. 11a). After 10 years, CO_2 -rich waters originated around the injection point move toward the zone 6, while a weakly acidic $\text{Ca}^{2+} - \text{HCO}_3^-$ (pH=6.9) solution mixes with neutral formation waters, originated by mineral hydrolysis, allowing the precipitation of secondary calcite (up to $+0.057\%$ by vol.; Fig. 12b). At 20 and 40 years (Fig. 12c,d), calcite balance remains negative only in the upper part of the zone 7 (-0.11% by vol.), while positive values (up to $+0.7\%$ by vol.) are recorded in the remaining sectors of the reservoir, i.e., inside ($+0.3$ – 0.69% by vol.), where acidic conditions persist (pH=5), and outside the plume ($+0.01$ – 0.3% by vol.).

The relatively high concentrations of HCO_3^- (0.068 mol/kg_w), due to both CO_2 and calcite dissolution coupled with that of chlorite, which releases Mg^{2+} in solution, favor the formation of disordered dolomite (Fig. 3a) as secondary mineral. Dolomite precipitation initiates after 1 year of injection ($+0.0013\%$ by vol.) just outside the CO_2 plume, where less

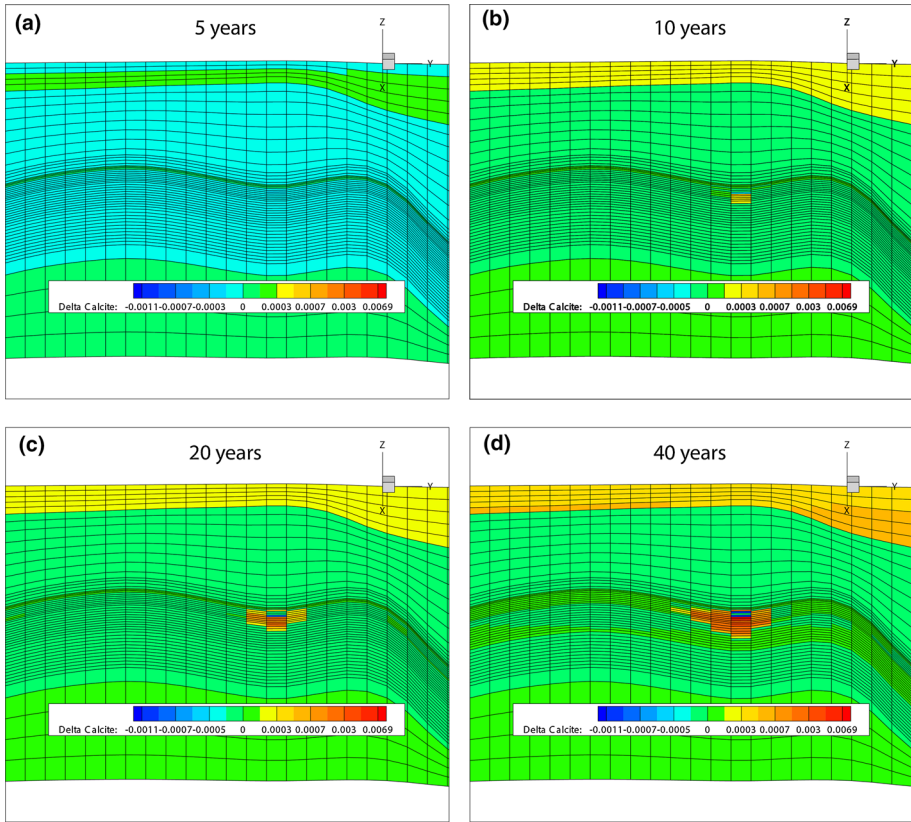


Fig. 12 Spatial distribution of delta (volume fraction change) calcite after 5 (a), 10 (b), 20 (c), and 40 (d) years of simulation in the structure reactive flow model. Grid spacing as in Fig. 9

acidic condition occurs, following the morphology of the layers in zone 7. After 20 years, newly formed dolomite (+0.0024 % by vol.) also occurs in the plume. At the end of the simulation, dolomite increases its volume up to 0.013 %. As a consequence of carbonate precipitation, the sequestered CO₂ (SMCO₂ in Fig. 13b) is positive (up to 7 kg of CO₂ per m³ of medium) with the exception of those cells close to the injection area (−1.3 kg m^{−3} of medium). Differently from the column model after 40 years the simulation has produced no precipitation of dawsonite.

The temporal evolution of other minerals in the reservoir, induced by the injection of CO₂, basically follows the same trend of the column model. Chlorite dissolves in the injection zone up to −0.05 % by vol., while laterally it moderately precipitates (0.008 % by vol.) (Fig. 14a). Illite (Fig. 14b) precipitates after 5 years (+0.0025 % by vol.) inside the CO₂ plume (pH=4.8) and after 40 years in the zone 7 (+0.012 % by vol.), following the boundary between zones 7 and 8, where a lower permeability layer is present (1.02×10^{-15} m²). Ca-montmorillonite and quartz (not shown) are very stable and notably react after 20 years and nearly at the end of the simulation. After 40 years, a small amount of these minerals precipitates (+0.095 and +0.002 % by vol., respectively) inside the injection zone, while at the boundary between the acidic and neutral zones they slightly dissolve (both −0.001 % by vol.). Among secondary minerals, initially not present in the system, kaolinite (not shown) precipitates inside the

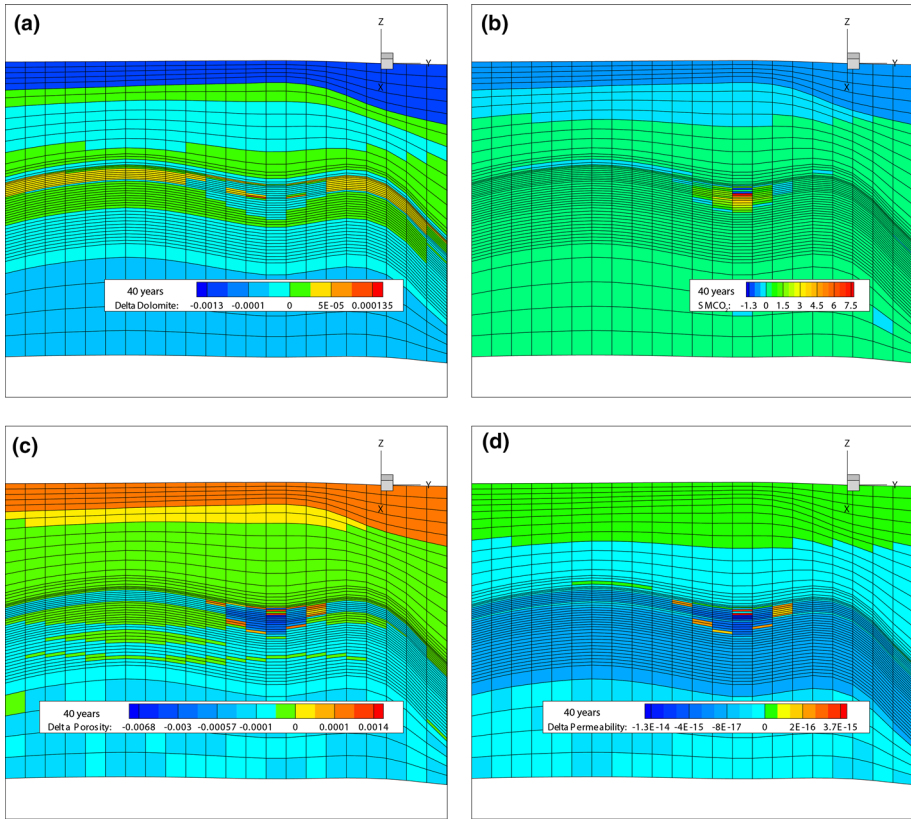


Fig. 13 Spatial distribution at 40 years of simulation of **a** delta disordered dolomite; **b** sequestered CO₂ (SMCO₂, kg of CO₂ sequestered per m³ of medium), **c** delta porosity, **d** delta permeability (m²) in the structure reactive flow model. Deltas refer to the volume fraction changes

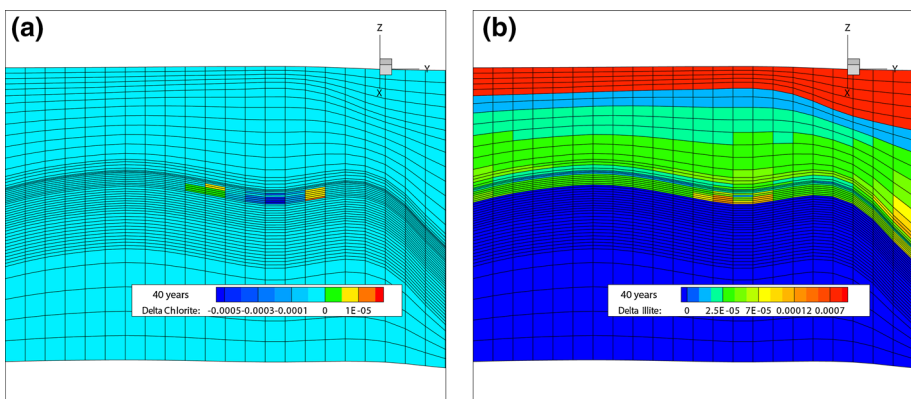


Fig. 14 Spatial distribution of **a** delta chlorite; **b** delta illite after 40 years of simulation in the structure (zoomed in the reservoir). Deltas are the volume fraction changes. Grid spacing as in Fig. 9

plume between 5 and 10 years of 0.003 % by vol. At the end of the simulation, a maximum of 0.02 % by vol. is formed in the zone 7. After 40 years, no phlogopite precipitates in the reservoir, and only a limited amount (0.00015 % by vol.) is found in the lowermost part of the caprock, likely due to water–rock interaction processes.

The kinetic reactions of minerals induced by CO₂ injection increase porosity up to +0.14 % by vol. in the injection zone (from 10 %, initial porosity, to 10.14 %), where the carbonate dissolution is higher and close to the CO₂ plume. Calcite re-precipitation and formation of secondary minerals cause a porosity decrease (−0.67 % by vol.) outside the plume in the zone 9 (from 10 to 9.3 %; Fig. 13c).

Permeability mimics the pattern shown by porosity, as it increases of $+3.7 \times 10^{-15} \text{ m}^2$ (from 2.34×10^{-14} to $2.71 \times 10^{-14} \text{ m}^2$) in the injection zone and in the surroundings of the CO₂ plume ($+2.7 \times 10^{-16}$). Mineral precipitation favors the permeability to significantly decrease in the middle part of the zone 7 (from 2.34×10^{-14} to $1.04 \times 10^{-14} \text{ m}^2$) and in the zone 9 (from 2.48×10^{-14} to $1.71 \times 10^{-14} \text{ m}^2$) (Fig. 13d).

A direct comparison between the hydrodynamic variables and the structure flow-only model was carried out with a simplified model where the sole calcite contribution to the geochemical reactions was taken into account. As pointed out for the column model, the calcite model does not fully consider the effect of the geochemical processes on the fluid flow. For numerical reasons, the structure reactive flow model requires relevant changes in the numerical model parameters, and this prevents a direct comparison with the flow-only model. Nevertheless, the most significant effects of the geochemical processes, also observed in the column reactive model, affecting the plume dimension and overpressure behavior, are below reported.

At the end of the injection, the CO₂ plume extents vertically for 240 m (from the lowermost layer of the zone 6 to the top of the zone 9), i.e., 40 m more than the flow-only model, and horizontally covers an area with a diameter of 3.5 km (Fig. 5a). Gas saturation shows a maximum value of 0.88. After 40 years, the plume diameter is 3.75 km with a downfall of 204 m (Fig. 15b), about 130 m larger than the flow-only model, likely due to the higher density of Ca²⁺-HCO₃[−]-rich solution.

The overpressure of the system is affected by both the effect of calcite precipitation and the decrease in porosity and permeability. After 20 years, an overpressure of $5.2 \times 10^6 \text{ Pa}$ is indeed recorded in the area surrounding the CO₂ plume and in the caprock ($+4.0 \times 10^6 \text{ Pa}$; Fig. 15c), i.e. $0.5 \times 10^6 \text{ Pa}$ higher than the flow-only model in the injection zone (i.e. $4.8 \times 10^6 \text{ Pa}$). After 40 years, an overpressure ranging from 3.5 to $4.5 \times 10^6 \text{ Pa}$ is present in the correspondence of the structural highs and in the main part of the reservoir (Fig. 15d).

The XCO_{2(aq)} distribution at 20 and 40 years displays very small changes with respect to the flow-only simulation. The downfall after 20 years is of about 475 m (from the top of the zone 6 to the middle part of the zone 9) while after 40 years is 430 m (from the top of the zone 6 to the middle part of the zone 9), covering an horizontal diameter of 4.5 km (Fig. 15e, f; 500 m wider than flow-only model).

Calcite (not shown) has a behavior similar to the full reactive model, dissolving −0.03 % by vol. in the injection cell, and re-precipitating of +0.13 % by vol. in the lower part of the zone 7 and in the zone 8. As calcite forms, porosity slightly increases of 0.015 % by vol. at the plume boundary, and it decreases of −0.12 % by vol. in the 8 zone (from 10 to 9.88 % by vol.). Permeability follows the same trend, decreasing of $-2.8 \times 10^{-15} \text{ m}^2$ in the zone 9 (from 2.48×10^{-14} to $2.2 \times 10^{-14} \text{ m}^2$). The distribution of CO_{2(aq)} in the structure is limited by the reduction of porosity and permeability. After 40 years, CO_{2(aq)} distributes horizontally with diameter of 4 km and a vertical development of 350 m (from the central part of the zone 6 to that of the zone 9). The values of pH (not shown) are positively correlated with those of

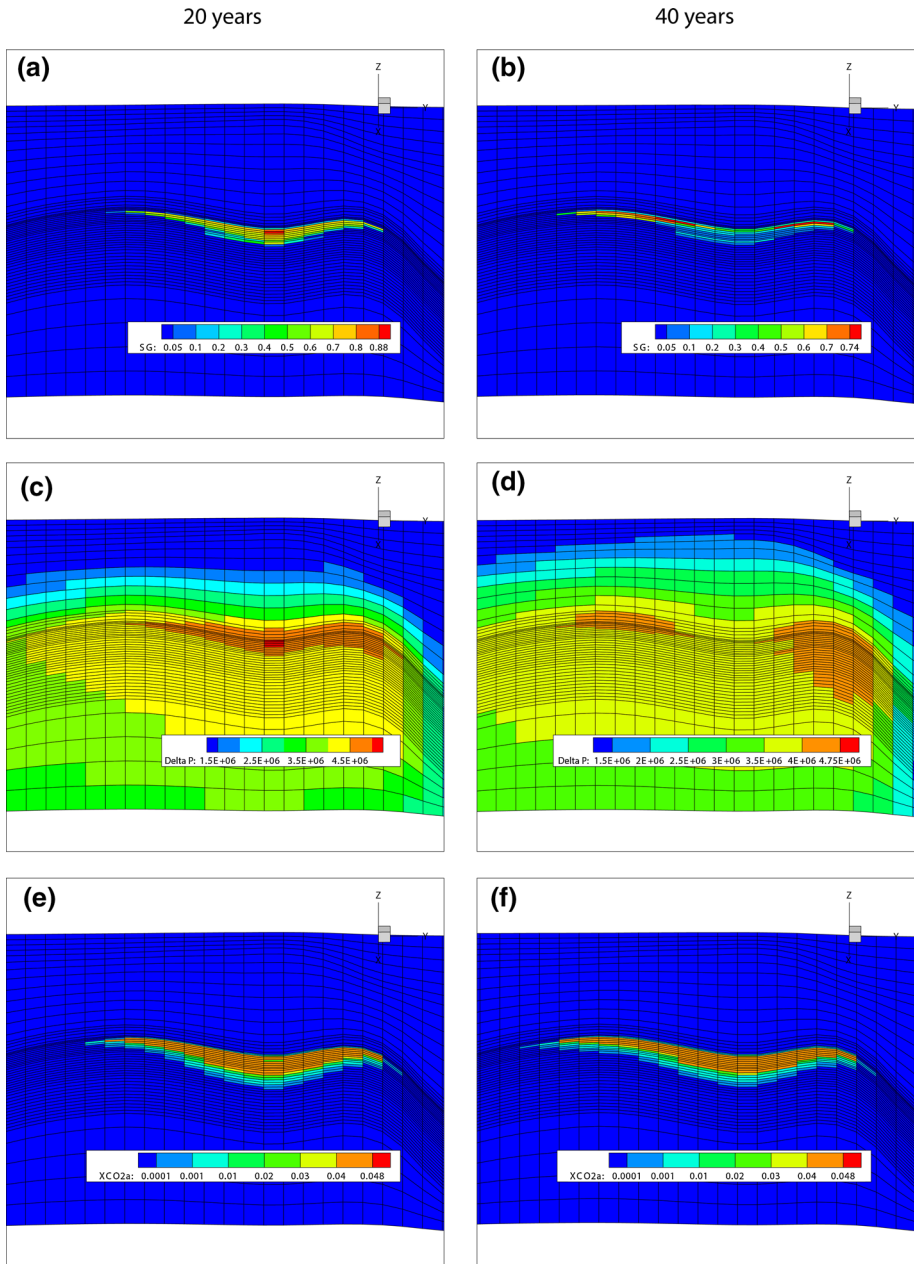


Fig. 15 Spatial distribution of gas saturation (SG) after 20 (a) and 40 years (b), overpressure (Pa) after 20 (c) and 40 years (d); aqueous CO₂ fraction (XCO_{2aq}) after 20 (e) and 40 years (f) into the structure calcite model. Grid spacing as in Fig. 9

CO_{2(aq)}, and are of 4.8 in the zones 6 and 7 and less acidic (~5.5) in the upper part of the zone 9. After 40 years, pH in the caprock is about 6.7.

Similarly to the column calcite model, the plume extension and the CO₂ impact on the reservoir result to be amplified with respect to the full reactive model.

7 Discussion

A real and complex structure, potentially suitable for CO₂ storage, was investigated at small and large scale by means of reactive transport simulations. The massive injection of CO₂ into the reservoir causes both disequilibrium among the present phases and changes in the fluid chemistry. Geochemical reactions (dissolution and or precipitation) produce variations in the solid phase volume leading to both flow and transport modifications in the porous media. Understanding the interplay between chemical reactions, rock geometry changes, and fluid transport properties is critical to achieve better predictions of the CO₂ fate in the reservoir rocks (e.g., [Noiriel et al. 2009](#)).

The numerical models conceived at the macroscopic scale can fail when the spatial arrangement of the minerals and pores is described (e.g., [Noiriel et al. 2009](#)). Thus, geometry is likely influencing the reactive transport. The effects deriving by the grid scaling on the chemical reactions were verified via two simulations at different scales.

In both the column and structure models, the carbonate reactions and their effects on porosity and permeability are by far the most important process. In the first months, porosity and permeability slightly increase close to the CO₂ injection well due to the fast reactivity of the carbonates. With time, salt-rich waters, originated by calcite dissolution close the injection well, move downward and mix with the formation waters causing the precipitation of secondary carbonates (mainly dolomite, as observed by [Xu et al. 2004](#); [Johnson et al. 2004, 2005](#); [Gaus et al. 2005](#); [Audigane et al. 2007](#); [Trémosa et al. 2014](#)). This process reduces porosity and permeability values (−0.67 % by vol. and -1.3×10^{-14} m², respectively; Fig. 13c, d), limiting the plume extent and increasing the overpressure throughout the system. Since calcite and dolomite are effective CO₂ sequestering minerals, the overall limiting factor is the availability of Ca²⁺ and Mg²⁺. Actually, the major amount of precipitated calcite is principally related to calcite dissolution in the injection zone and not to a newly formed mineral since no additional source of Ca²⁺ is present. Deposition of calcite occurs at the boundary between acidic fluids and formation waters due to water stratification. This process is favored by the original low permeability of the limestone formations characterizing the reservoir (Table 3). The restrictive factors of CO₂ injection in such a system are both the low velocity of the displaced water and the overpressure needed to provide the expected injection rate. The former processes are empathized in the structure model with respect to the column simulation, due to both the smaller scale and the reduced amount of injected CO₂ (1,500 t per 1 year vs. 1.5 Mt per 20 years).

Geochemical reactions of reservoir minerals induced by the injection of CO₂ essentially show the same evolution in both the column and the structure models. Nevertheless, some differences in time and extent of reactions are observed. The amount of dissolved CO₂ in the formation water is determined by solubility as well as by transport processes due to migration of CO₂. At a larger scale, the migration of CO₂ (i.e., structure model) leads to a large reservoir volume with low concentrations of CO_{2(aq)} ([Klein et al. 2013](#)). On the contrary, at a smaller scale, less water is in contact with the same amount of minerals. Thus, a limited amount of dissolved CO₂ is requested to achieve saturation. This turns into faster reactions although the overall amount of mineral precipitation decreases ([Klein et al. 2013](#)).

This process is evident when the behavior of dawsonite is considered. In the column model, this secondary mineral starts to precipitate after 10 years from the injection of CO₂, whereas after 40 years, no dawsonite forms in the structure model. This effect can be due to both the different scale of the two systems affecting the fluid transport and the dilution process, which may modify the chemical concentrations. Dawsonite is reported to be abundant in natural CO₂ reservoirs ([Smith and Milton 1966](#); [Baker et al. 1995](#); [Pearce et al. 1996](#); [Moore et al. 2005](#);

Worden 2006; Golab et al. 2006, 2007; Pauwels et al. 2007; Gao et al. 2009; Liu et al. 2011) and according to different geochemical models (e.g., Johnson et al. 2001; Gaus et al. 2005; Audigane et al. 2007; Xu et al. 2005) it is considered a key mineral in permanently trapping significant amounts of CO₂. However, in the last few years, several studies (e.g., Bénézech et al. 2007; Hellevang et al. 2011) suggested that the precipitation of dawsonite is subjected to tight constraints, as it becomes unstable as reservoir pressure decreases after the injection of CO₂. This behavior is consistent with what observed in the column model, where newly formed dawsonite completely dissolves after 20 years from the end of injection. We are aware that inclusions of dawsonite in secondary minerals can produce an optimistic prediction for mineral trapping, although this does not produce a positive feedback by current scientific evidences. The geochemical and mineralogical evolution of the CO₂-hosting reservoir can be addressed to three main regions: a) inside the CO₂ plume, b) outside of it, and c) at the boundary between the two.

- Inside the CO₂ plume, where highly acidic conditions persist (pH is from 4.7 to 5.2, CO_{2(aq)} from 1.14 to 0.3 mol/kg_w), calcite dissolves together with chlorite (e.g. Black and Haese 2014), increasing both the respective porosity and permeability. In this zone, the formation of clay minerals (illite, kaolinite, and phlogopite-like mica) occurs.
- Outside the plume, where neutral conditions (pH > 6.7) are present, geochemical reactions are mainly controlled by “ordinary” water–rock interaction.
- At the boundary between the acidic and neutral zone, where less acidic conditions are present (pH is from 5.2 to 6.7 and CO_{2(aq)} is from 0.15 to 0.003 mol/kg_w), dissolved calcite can re-precipitate (calcite displacement) together with dolomite and chlorite, provoking a decrease in porosity and permeability. The behavior of calcite may be regarded as “displacement” from the CO₂-rich waterfront to the downstream fluid path, and this is likely the main cause of porosity/permeability reduction. This geochemical barrier diminishes the outflow velocity of the CO₂-displaced water, producing a lower CO₂ injectivity.

The present study was applied to a real reservoir located offshore the Tyrrhenian coast of central Italy, which is characterized by specific physico-chemical features and suitable for numerical simulations. Some assumptions and estimations of the missing parameters are required, particularly because no drilling core samples are available, and our statements were mainly based on inland outcropping rocks.

Furthermore, the evolution of the surface area in geological media is very complex, and its impact on the results could be of several orders of magnitude (e.g., Gautier et al. 2001; Zerai et al. 2006). Estimated mineral dissolution rates cover a wide range of values for each species. Processes ruling dissolutions were extensively studied and quantified, although similar approaches rarely consider CO₂ saturated systems.

Despite the fact that the quality of experimental data and assumptions may strongly affect the reliability of numerical models, it is important to highlight that they represent a simplified model of the real system. They can be used to formulate and/or support hypotheses concerning the involved processes, although they do not allow unconditioned predictions.

8 Conclusions

3D numerical simulations of reactive transport of CO₂ into an offshore carbonatic structure of central Italy was performed at different scales to evaluate: i) the geochemical evolution at

the reservoir–caprock interface, ii) the porosity and permeability variations, and iii) the CO₂ path from the injection well throughout the geological structure.

The main results achieved in this study can be summarized, as follows:

- By coupling geochemical reactions and fluid flow processes, the dissolution of calcite close to the injection zone, and the precipitation of secondary calcite and minor dolomite at the boundary between the acidic and neutral zone, where less acidic conditions prevail, were observed. Clay minerals formations (e.g., illite and kaolinite) occur inside the plume where there are more acidic conditions.
- The effect of the carbonate dissolution/precipitation on porosity and permeability is by far the most important process. At the injection point, these two parameters increase of +0.14 % and $+3.7 \times 10^{-15} \text{ m}^2$, respectively. A geochemical barrier forms downstream along the fluid flow path causing a decrease in terms of porosity (−0.68 %) and permeability ($-1.3 \times 10^{-14} \text{ m}^2$).
- The geochemical (carbonatic) barrier reduces the outflow velocity of the CO₂–displaced water. In the column model, a reduction of the plume size (−43 % by vol.) is observed when comparing the flow-only and the reactive flow models after 100 years. A reduction of SG values (0.20 vs. 0.11) was recorded in the calcite model. A similar behavior is shown in the structure model. Although not directly comparable with the flow-only model, the reduction of CO₂ plume (about 60 % by vol.) in the reactive flow model can be considered meaningful.
- This ‘barrier’ induces a lower CO₂ injectivity, which is highlighted when comparing the structure flow-only and the calcite models, where an overpressure increase from 4.8 to $5.3 \times 10^6 \text{ Pa}$ is observed. This phenomenon may have an effective impact on the sequestration of CO₂ due to the reduction of the available storage volume reached by the CO₂ plume in 20 years and/or to the enhancement of the required injection pressure.

Despite the limitations and assumptions, which are inevitably applied to geochemical and numerical modeling, our results stress the usefulness of this approach in estimating the fate of CO₂ in saline aquifers.

Acknowledgments The authors wish to express their gratitude to Elena Pecchioni, Federico Lucci, Andrea Cavallo for their help during XRD, petrographic, and SEM-EDS analyses, respectively. Gianfranco Galli is warmly thanked for his assistance in the various shell scripting and Gabriele Biccocchi for his support in the early stage of the model. Many thanks are due to Luca Pizzino, Alessandra Sciarra, and Monia Procesi for their useful suggestions. Authors would like to greatly thank SMT Microtechnology Company for providing an educational license of Kingdom suite software, used for seismic interpretation and 3D modeling. We wish to express our gratitude to M.J. Blunt, Associate Editor, and three anonymous reviewers for their suggestions and comments, which greatly improved an early version of the manuscript.

References

- Agosta, F., Prasad, M., Aydin, A.: Physical properties of carbonate fault rocks, fucino basin (Central Italy): implications for fault seal in platform carbonates. *Geofluids* **7**, 19–32 (2007)
- Allen, D.E., Strazisar, B.R., Soong, Y., Hedges, S.W.: Modeling carbon dioxide sequestration in saline aquifers: significance of elevated pressures and salinities. *Fuel Process. Technol.* **86**(14–15), 1569–1580 (2005)
- André, L., Audigane, P., Azaroual, M., Menjöz, A.: Numerical modeling of fluid: rock chemical interactions at the supercritical CO₂–liquid interface during CO₂ injection into a carbonate reservoir, the Dogger aquifer (Paris Basin, France). *Energy Convers. Manag.* **48**, 1782–1797 (2007)
- Audigane, P., Gaus, I., Czernichowski-Lauriol, I., Pruess, K., Xu, T.: Two-dimensional reactive transport modeling of CO₂ injection in a saline aquifer at the Sleipner site, North Sea. *Am. J. Sci.* **307**, 974–1008 (2007)

- Audigane, P., Oldenburg, C.M., van der Meer, B., Geel, K., Lions, J., Gaus, I., Robelin, Ch. I., Durst, P., Xu, T.: Geochemical modeling of the CO₂ injection into a methane gas reservoir at the K12-B Field, North Sea. In: Grobe, M., Pashin, J. C., Dodge, R. L. (eds.), *Carbon dioxide Sequestration in Geological Media-State of the Science*. AAPG Studies, pp. 1–20. (2008)
- Bachu, S., Adams, J.J.: Sequestration of CO₂ in geological media in response to climate change: capacity of deep saline aquifers to sequester CO₂ in solution. *Energy Convers. Manag.* **44**(20), 3151–3175 (2003)
- Baker, J.C., Bai, G.P., Hamilton, P.J., Golding, S.D., Keene, J.B.: Continental-scale magmatic carbon dioxide seepage recorded by dawsonite in the Bowen–Gunnedah–Sydney Basin system Eastern, Australia. *J. Sediment Res. A* **65**(3), 522–530 (1995)
- Balashov, V.N., Guthrie, G.D., Hakala, J.A., Lopano, C.L., Rimstidt, J.D., Brantley, S.L.: Predictive modeling of CO₂ sequestration in deep saline sandstone reservoirs: impacts of geochemical kinetics. *Appl. Geochem.* **30**, 41–56 (2013)
- Bartole, R.: Tectonic structures of the Latian–Campanian shelf [Tyrrhenian sea]. *Boll. Ocean. Teor. Appl.* **2**, 197–230 (1984)
- Bartole, R.: Caratteri sismostratigrafici, strutturali e paleogeografici della piattaforma continentale toscolaziale; suoi rapporti con l’Appennino settentrionale. *Boll. Soc. Geol. Ital.* **109**, 599–622 (1990)
- Bartole, R.: The North Tyrrhenian–Northern Apennines postcollisional system: constraints for geodynamic model. *Terra Nova* **7**, 7–30 (1995)
- Berner, R.A., Holdren, G.R.: Mechanism of feldspar weathering. II: Observations of feldspars from soils. *Geochim. Cosmochim. Acta.* **43**, 1173–1186 (1979)
- Berner, R.A., Schott, J.: Mechanism of pyroxene and amphibole weathering. II. Observations of soil grains. *Am. J. Sci.* **282**, 1214–1231 (1982)
- Bénézech, P., Palmer, D.A., Anovitz, L.M., Horita, J.: Dawsonite synthesis and reevaluation of its thermodynamic properties from solubility measurements: implications for mineral trapping of CO₂. *Geochim. Cosmochim. Acta.* **71**, 4438–4455 (2007)
- Black, J.R., Haese, R.R.: Chlorite dissolution rates under CO₂ saturated conditions from 50 to 120 °C and 120 to 200 bar CO₂. *Geochim. Cosmochim. Acta* **125**, 225–240 (2014)
- Bumb, P., Quattrocchi, F., Desideri, U., Arcioni, L.: Cost optimized CO₂ pipeline transportation grid: a case study from Italian industries. *World Acad. Sci. Eng. Technol.* **58**, 138–145 (2009)
- Buttinelli, M., Procesi, M., Cantucci, B., Quattrocchi, F., Boschi, E.: The geo-database of caprock quality and deep saline aquifers distribution for geological storage of CO₂ in Italy. *Energy* **36**(5), 1–16 (2011)
- Buttinelli, M., Scrocca, D., De Rita, D., Quattrocchi, F.: Modes of stepwise eastward migration of the Northern Tyrrhenian Sea back-arc extension: evidences from the Northern Latium offshore (Italy). *Tectonics* **33**, 187–206 (2014)
- Cantucci, B., Montegrossi, G., Vaselli, O., Tassi, F., Quattrocchi, F., Perkins, E.H.: Geochemical modeling of CO₂ storage in deep reservoirs; the Weyburn Project (Canada). *Chem. Geol.* **265**, 181–197 (2009)
- Carminati, E., Doglioni, C., Scrocca, D.: Alps versus Apennines. In: *Special Volume of the Italian Geological Society for the 32^o International Geological Congress, Florence*, pp. 141–151 (2004).
- Cataldi, R., Mongelli, F., Squarci, P., Taffi, L., Zito, G., Calore, C.: Geothermal ranking of Italian territory. *Geothermics* **1995**(24), 115–129 (1995)
- Chiarabba, C., Jovane, L., Di Stefano, R.: A new view of Italian seismicity using 20 years of instrumental recordings. *Tectonophysics* **395**, 251–268 (2005)
- Chiodini, G., Frondini, F., Cardellini, C., Parello, F., Peruzzi, L.: Rate of diffuse carbon dioxide earth degassing estimated from carbon balance of regional aquifers: the case of central Apennine, Italy. *J. Geophys. Res.* **105**, 8423–8434 (2000)
- Chiodini, G., Frondini, F., Ponziani, F.: Deep structures and carbon dioxide degassing in central Italy. *Geothermics* **24**(1), 81–94 (1995)
- Clauser, C.: Geothermal energy. In: K. Heinloth (ed.), *Landolt-Börnstein, Group VIII: Advanced Materials and Technologies, Vol. 3 Energy Technologies, Subvol. C: Renewable Energies*, pp. 480–595. Springer, Heidelberg–Berlin (2006)
- Clauser, C., Huenges, E.: Thermal Conductivity of Rocks and Minerals, Chapter 3 of *A Handbook of Physical Constants*. AGU Ref. Shelf 3 (1995)
- Corey, A.T.: The interrelation between gas and oil relative permeabilities. *Prod. Mon.* **19**, 38 (1954)
- Damen, K., Martijn, V.T., Faaij, A., Turkenburg, W.: A comparison of electricity and hydrogen production systems with CO₂ capture and storage. Part A: Review and selection of promising conversion and capture technologies. *Prog. Energy Combust.* **32**, 215–246 (2006)
- Dewey, J.F., Helman, M.L., Turco, E., Hutton, D.H.W., Knott, S.D.: Kinematics of the western Mediterranean. In: Coward, M.P., Dietrich, D., Park, R.G. (eds.) *Alpintectonics*, pp. 265–283. Geological Society of London, London (1989)

- Donda, F., Volpi, V., Persoglia, S., Parushev, D.: CO₂ storage potential of deep saline aquifers: the case of Italy. *Int. J. Greenh. Gas Control* **5**, 327–335 (2011)
- Duncan, I.: Carbon sequestration risks, opportunities and learning from the CO₂-EOR industry. Texas: University of Austin. US House Committee on Energy and Commerce, Sub-comm on Energy and the Environment (2009)
- Ennis-King, J., Paterson, L.: Rate of dissolution due to convective mixing in the underground storage of carbon dioxide. In: Gale, J., Kaya, Y. (eds.) 6th International Conference on Greenhouse Gas Control Technologies, pp. 507–510. Pergamon (2003)
- Fazzini, P., Gelmini, R., Mantovani, M.P., Pellegrini, M.: Geologia dei Monti della Tolfa (Lazio Settentrionale, provincie di Viterbo e Roma). *Memorie della Società Geologica Italiana* **11**, 65–144 (1972)
- Frank, M.J.W., Kuipers, J.A.M., Van Swaaij, W.P.M.: Diffusion coefficients and viscosities of CO₂ + H₂O, CO₂ + CH₃OH, NH₃ + H₂O, and NH₃ + CH₃OH liquid mixtures. *J. Chem. Eng. Data* **41**, 297–302 (1996)
- Fritz, B.: Multicomponent solid solution for clay minerals and computer modeling of weathering processes. *Chem. Weather. Nato ASI Ser.* **149**, 9–34 (1985)
- Garcia, J.E.: Density of aqueous solutions of CO₂. Lawrence Berkeley National Laboratory Paper LBNL-49023. University of California (2001)
- Gao, Y., Liu, L., Hu, W.: Petrology and isotopic geochemistry of dawsonite-bearing sandstones in Hailaer basin, northeastern China. *Appl. Geochem.* **24**(9), 1724–1738 (2009)
- Gaus, I., Audigane, P., Andre, L., Lions, J., Jacquemet, N., Dutst, P., Czernichowski-Lauriol, I., Azaroual, M.: Geochemical and solute transport modelling for CO₂ storage, what to expect from it? *Int. J. Greenh. Gas Control* **2**(4), 605–625 (2008)
- Gaus, I., Azaroual, M., Czernichowski-Lauriol, I.: Reactive transport modelling of the impact of CO₂ injection on the clayey cap rock at Sleipner (North Sea). *Chem. Geol.* **217**, 319–337 (2005)
- Gautier, J.M., Oelkers, E.H., Schott, J.: Are quartz dissolution rates proportional to B.E.T. surface areas? *Geochim. Cosmochim. Acta* **65**, 1059–1070 (2001)
- Golab, A.N., Carr, P.F., Palamara, D.R.: Influence of localised igneous activity on cleat dawsonite formation in Late Permian coal measures, Upper Hunter Valley, Australia. *Int. J. Coal Geol.* **66**, 296–304 (2006)
- Golab, A.N., Hutton, A.C., French, D.: Petrography, carbonate mineralogy and geochemistry of thermally altered coal in Permian coal measures, Hunter Valley, Australia. *Int. J. Coal Geol.* **70**(1–3), 150–165 (2007)
- Grandstaff, D.E.: Changes in surface area and morphology and the mechanism of forsterite dissolution. *Geochim. Cosmochim. Acta* **42**, 1899–1901 (1978)
- Gundogan, O., Mackay, E., Todd, A.: Comparison of numerical codes for geo-chemical modelling of CO₂ storage in target sandstone reservoirs. *Chem. Eng. Res. Des.* **89**(9), 1805–1816 (2011)
- Gunter, W.D., Bachu, S., Benson, S.M.: The role of hydrogeological and geochemical trapping in sedimentary basins for secure geological storage for carbon dioxide. In: Baines, S.J., Worden, R.H. (eds.) *Geological Storage of Carbon Dioxide*, vol. 233, pp. 129–145. Geological Society Special Publication, London (2004)
- Gunter, W.D., Perkins, E.H., Hutcheon, I.: Aquifer disposal of acid gases: modeling of water–rock reactions for trapping of acid wastes. *Appl. Geochem.* **15**, 1085–1095 (2000)
- Gunter, W.D., Perkins, E.H., McCann, T.J.: Aquifer disposal of CO₂-rich gases: reaction design for added capacity. *Energy Convers. Manag.* **34**, 941–948 (1993)
- Hashimoto, S., Suzuki, M.: Vertical distribution of carbon dioxide diffusion coefficients and production rates in forest soils. *Soil. Sci. Soc. Am. J.* **66**, 1151–1158 (2002)
- Helgeson, H.C., Kirkham, D.H., Flowers, G.C.: Theoretical prediction of the thermodynamic behavior of aqueous electrolytes at high pressures and temperatures: IV. Calculation of activity coefficients, osmotic coefficients, and apparent molal and standard and relative partial molal properties to 600 °C and 5 kb. *Am. J. Sci.* **281**, 1249–1516 (1981)
- Hellevang, H., Declercq, J., Aagaard, P.: Why is dawsonite absent in CO₂ charged reservoirs? *Oil Gas Sci. Technol.* **66**, 119–135 (2011)
- Hitchon, B., Gunter, W.D., Gentzis, T., Bailey, R.T.: Sedimentary basins and greenhouse gases: a serendipitous association. *Energy Convers. Manag.* **40**(8), 825–843 (1999)
- Holloway, S.: *The Underground Disposal of Carbon Dioxide*, Final Report of JOULE II Project No. CT92-0031. British Geological Survey (1996)
- Holloway, S.: Storage of fossil fuel derived carbon dioxide beneath the surface of the Earth. *Ann. Rev. Energy Environ.* **26**, 145–166 (2001)
- Horvath, F., Berckheimer, H.: Mediterranean backarc-basins. In: Berckheimer H., Hsü K. (eds.) *Alpine-Mediterranean-geodynamics*. AGU geodynamics series, 141–163 (1982)
- IEA, *Technology roadmap: Carbon capture and storage*. Special publication (2009)

- Izgec, O., Demiral, B., Bertin, H., Akin, S.: Experimental and numerical investigation of carbon sequestration in deep saline aquifers. In: SPE/EPA/DOE Exploration and Production Environmental Conference, Galveston, SPE Paper 94697 (2005)
- Izgec, O., Demiral, B., Bertin, H., Akin, S.: CO₂ injection into saline carbonate aquifer formations II: comparison of numerical simulations to experiments. *Transp. Porous Media* **73**, 57–74 (2007)
- Johnson, J.W., Nitao, J.J., Steefel, C.I., Knauss, K.G.: Reactive transport modeling of geologic CO₂ sequestration in saline aquifers: the influence of intra-aquifer shales and the relative effectiveness of structural, solubility, and mineral trapping during prograde and retrograde sequestration. First National Conference on Carbon Sequestration. May 14–17, 2001, Washington, D.C., 60 (2001)
- Johnson, J.W., Nitao, J.J., Knauss, K.G.: Reactive transport modelling of CO₂ storage in saline aquifers to elucidate fundamental processes, trapping mechanisms and sequestration partitioning. *Geol. Soc. Lond. Spec. Publ.* **233**(1), 107–128 (2004)
- Johnson, J.W., Nitao, J.J., Morris, J.P.: Reactive transport modeling of cap rock integrity during natural and engineered CO₂ storage, Carbon Dioxide Capture for Storage in Deep Geologic Formations - Results from the CO₂ Capture Project, v. 2: Geologic Storage of Carbon Dioxide with Monitoring and Verification, S.M. Benson, (ed.), Elsevier, London, pp. 787–814 (2005)
- Johnson, J.W., Oelkers, E.H., Helgeson, H.C.: SUPCRT 92: a software package for calculating the standard molal thermodynamic properties of minerals, gases, aqueous species, and reactions from 1 to 5000 bars and 0 to 1000 °C. *Comput. Geosci.* **18**, 899–947 (1992)
- Jones, D.J., Beaubien, S.E., Baubron, J.C., Cinti, D., Davis, J.R., Emery, C. et al.: Continued soil gas monitoring at the Weyburn unit in 2004. Report No. COAL R288 DTI/Pub URN 05/1261 (2006)
- Klein, E., De Lucia, M., Kempka, T., Kühn, M.: Evaluation of long-term mineral trapping at the Ketzin pilot site for CO₂ storage: an integrative approach using geochemical modelling and reservoir simulation. *Int. J. Greenh. Gas Control* **19**, 720–730 (2013)
- Kuhn, M., Chiang, W.-H.: Processing Shemat, Ver. 4.0.0, SHEMAT Ver. 8.0, J. Bartels, C. Clauser, M. Kuhn, D. Mottaghy, V. Rath, R. Wagner & A. Wolf, Springer-Verlag, Berlin, Heidelberg (2003)
- Lasaga, A.C.: Chemical kinetics of water–rock interactions. *J. Geophys. Res.* **89**, 4009–4025 (1984)
- Lasaga, A.C.: Fundamental approaches in describing mineral dissolution and precipitation rates. In: White, A.F., Brantley, S.L. (eds.) *Chemical Weathering Rates of Silicates Minerals*, Reviews in Mineralogy 31, pp. 23–86. BookCrafters, Chelsea (1995)
- Lasaga, A.C., Soler, J.M., Ganor, J., Burch, T.E., Nagy, K.L.: Chemical weathering rate laws and the global cycles. *Geochim. Cosmochim. Acta* **58**(10), 2361–2386 (1994)
- Lichtner, P.C.: Continuum formulation of multicomponent-multiphase reactive transport. In: Lichtner, P.C., Steefel, C.I., Oelkers, E.H. (eds.) *Reactive Transport in Porous Media*, vol. 34. Mineralogical society of America, Washington DC (1996)
- Liu, N., Liu, L., Qu, X., Yang, H., Wang, L., Zhao, S.: Genesis of authigenic carbon-ate minerals in the Upper Cretaceous reservoir, Honggang Anticline, Songliao Basin: a natural analog for mineral trapping of natural CO₂ storage. *Sediment. Geol.* **237**(3–4), 166–178 (2011)
- Lutterotti, L., Matthies, S., Wenk, H.-R.: MAUD (Material Analysis Using Diffraction): a user friendly leakage, therefore a major effort should be done in order to study this kind of systems. Java program for Rietveld Texture Analysis and more, Proceeding of the Twelfth International Conference on Textures of Materials (ICOTOM-12), 1, 159 (1999)
- Metz, B., Davidson, O.R., Bosch, P.R., Dave, R., Meyer, L.A.: In: Contribution of Working Group III to the Fourth Assessment Report of the Intergovernmental Panel on Climate Change. UK & USA: IPCC, Cambridge University Press, Cambridge (2007)
- Metz, B., Davidson, O., de Coninck, H., Loos, M., Meyer, L.: Carbon dioxide capture and storage. Intergovernmental panel on climate change. In: Chapter 5: underground geological storage. UK: IPCC, Cambridge University Press, Cambridge (2005)
- Marini, L.: Geological Sequestration of Carbon Dioxide: Thermodynamics, Kinetics, and Reaction Path Modeling. *Developments in Geochemistry*. Elsevier Science, New York (2007)
- Millington, R.J., Quirk, J.P.: Permeability of porous solids. *Trans. Faraday Soc.* **57**, 1200–1207 (1961)
- Milly, P.C.D.: Moisture and heat transport in hysteretic, inhomogeneous porous media: a matric-head based formulation and a numerical model. *Water Resour. Res.* **18**(3), 489–498 (1982)
- Minissale, A.: Origin, transport and discharge of CO₂ in Central Italy. *Earth Sci. Rev.* **66**, 89–141 (2004)
- Moghadas, J., Müller-Steinhagen, H., Jamialahmadi, M., Sharif, A.: Model Study on the kinetics of oil formation damage due to salt precipitation from injection. *J. Pet. Sci. Eng.* **46**(4), 299–299 (2005)
- Moore, J., Adams, M., Allis, R., Lutz, S., Rauzi, S.: Mineralogical and geochemical consequences of the long-term presence of CO₂ in natural reservoirs: an example from the Springerville-St. Johns Field, Arizona, and New Mexico, USA. *Chem. Geol.* **217**, 365–385 (2005)

- Morettini E., Santantonio M., Bartolini A., Cecca F., Baumgartner P.O., Hunziker J.C.: Carbon isotope stratigraphy and carbonate production during the Early-Middle Jurassic: examples from the Umbria-Marche-Sabina Apennines (central Italy). *Palaeogeography, Palaeoclimatology, Palaeoecology*. **184**, 251–273 (2002)
- Montegrossi, G., Cantucci, B., Vaselli, O., Quattrocchi, F.: Reconstruction of porosity profile in an off-shore well. *Bollettino di Geofisica Teorica ed Applicata* **49**(2), 408–410 (2008)
- Narasimhan, T.N., Witherspoon, P.A.: An integrated finite difference method for analyzing fluid flow in porous media. *Water Resour. Res.* **12**, 57–64 (1976)
- Nghiem, L., Sammon, P., Grabenstetter, J., Ohkuma, H.: Modeling CO₂ storage in aquifers with a fully-coupled geochemical EOS compositional simulator. In: *SPE/DOE Symposium on Improved Oil Recovery*, 7–21 April 2004, Tulsa, SPE 89474 (2004)
- Noiriel, C., Luquot, L., Made, B., Raimbault, L., Gouze, P., van der Lee, J.: Changes in reactive surface area during limestone dissolution: an experimental and modeling study. *Chem. Geol.* **265**, 160–170 (2009)
- Obi, E.-O., Blunt, M.J.: Streamline-based simulation of carbon dioxide storage in a North Sea aquifer. *Water Resour. Res.* **42** (2006)
- Palandri, J.L., Kharaka, Y.K.: A Compilation of Rate Parameters of Water-Mineral Interaction Kinetics for Application to Geo-chemical Modeling: U.S. Geological Survey Water-Resources Investigations Report 04–1068 (2004)
- Palmer, B.J.: Calculation of thermal-diffusion coefficients from plane-wave fluctuations in the heat energy density. *Phys. Rev. E* **49**(3), 2049–2057 (1994)
- Pape, H., Clauser, C., Iffland, J.: Permeability prediction based on fractal pore-space geometry. *Geophysics* **64**(5), 1447–1460 (1999)
- Parkhurst, D.L., Appelo, C.A.J.: User's Guide to PHREEQC (Version 2)—A Computer Program for Speciation, Batch-reaction, One-dimensional Transport, and inverse geochemical calculations. In: U. S. Geological Survey Water-Resources Investigations Report 99–4259 (1999)
- Pauwels, H., Gaus, I., le Nindre, Y.M., Pearce, J., Czernichowski-Lauriol, I.: Chemistry of fluids from a natural analogue for a geological CO₂ storage site (Montmiral, France): Lessons for CO₂-water-rock interaction assessment and monitoring. *Appl. Geochem.* **22**, 2817–2833 (2007)
- Pearce, J.M., Holloway, S., Wacker, H., Nelis, M.K., Rochelle, C., Bateman, K.: Natural occurrences as analogues for the geological disposal of carbon dioxide. *Energy Convers. Manag.* **37**, 1123–1128 (1996)
- Procesi, M., Cantucci, B., Buttinelli, M., Armezzani, G., Quattrocchi, F., Boschi, E.: Strategic use of the underground in an energy mix plan: synergies among CO₂, CH₄ geological storage and geothermal energy. Latium Region case study (Central Italy). *Appl. Energy* **110**, 104–131 (2013)
- Pruess, K.: Numerical studies of fluid leakage from a geologic disposal reservoir for CO₂ show self-limiting feedback between fluid flow and heat transfer. Lawrence Berkeley National Laboratory, Paper LBNL-57362 (2005)
- Pruess, K., García, J.: Multiphase flow dynamics during CO₂ injection into saline aquifers. *Environ. Geol.* **42**, 282–295 (2002)
- Quattrocchi, F., Cantucci, B., Cinti, D., Galli, G., Pizzino, L., Sciarra, A.: Continuous/ discrete geochemical monitoring of CO₂ natural analogues and of diffuse degassing structures (DDS): hints for CO₂ storage sites geochemical protocol. *Energy Proc.* **1**, 2135–2142 (2008)
- Raffensperger, J.P.: Numerical simulation of sedimentary basin-scale hydrochemical processes. In: Corapcioglu, Y.C. (ed.) *Advances in Porous Media*, p. 440. Elsevier Science, Amsterdam (1996)
- Robertson, E.C.: Thermal properties of rocks, U.S.G.S. Open file report 88–441, 106 pp., U.S. Geological Survey, Reston, Va. (1988)
- Rosembaum, G., Lister, G.S., Duboz, C.: Reconstruction of the tectonic evolution of the western Mediterranean since the Oligocene. In: Rosembaum, G., Lister, G.S. (eds.) *Reconstruction of the Evolution of the Alpine-Himalayan Orogeny*, vol. 8, pp. 107–130. Geoscience Publishing Ltd, Alta (2002)
- Rutqvist, J., Tsang, C.-F.: A study of caprock hydromechanical changes associated with CO₂ injection into a brine aquifer. *Environ. Geol.* **42**, 296–305 (2002)
- Schaefer, H.T., Mcgrail, B.P., Owen, A.T.: Carbonate mineralization of volcanic province basalts. *Int. J. Greenh. Gas Control* **4**, 249–261 (2010)
- Scrocca, D., Doglioni, C., Innocenti, F.: Constraints for an interpretation of the Italian geodynamics: a review. In: Scrocca, D., Doglioni, C., Innocenti, F., Manetti, P., Mazzotti, A., Bertelli, L., Burbi, L., Doffizi, S. (eds.) *CROP Atlas: Seismic Reflection Profiles of the Italian Crust*, vol. 62, pp. 15–46. *Memorie Descrittive della Carta Geologica d'Italia*, Rome (2003)
- Singh, T.N., Sinha, S., Singh, V.K.: Prediction of thermal conductivity of rock through physico-mechanical properties. *Build. Environ.* **42**, 146–155 (2007)
- Smith, J.W., Milton, C.: Dawsonite in the green river formation of Colorado. *Econ. Geol.* **61**, 1029–1042 (1966)

- Spycher, N., Pruess, K.: CO₂–H₂O mixtures in the geological sequestration of CO₂. II. Partitioning in chloride brines at 12–100°C and up to 600 bar. *Geochim. Cosmochim. Acta* **69**, 3309–3320 (2005)
- Sonnenthal, E., Ito, A., Spycher, N., Yui, M., Apps, J., Sugita, Y., Conrad, M., Kawakami, S.: Approaches to modeling coupled thermal, hydrological, and chemical processes in the Drift Scale Heater Test at Yucca Mountain. *Int. J. Rock Mech. Min. Sci.* **42**, 6719–6987 (2005)
- Soong, Y., Goodman, A.L., McCarthy-Jones, J.R., Baltrus, J.P.: Experimental and simulation studies on mineral trapping of CO₂ with brine. *Energy Convers. Manag.* **45**, 1845–1859 (2004)
- Steeffel, C.L., Lasaga, A.C.: A coupled model for transport of multiple chemical species and kinetic precipitation/dissolution reactions with applications to reactive flow in single phase hydrothermal system. *Am. J. Sci.* **294**, 529–592 (1994)
- Tamini, A., Rinker, B., Sandall, O.C.: Diffusion coefficients for hydrogen sulfide, carbon dioxide, and nitrous oxide in water over the temperature range 293–368 K. *J. Chem. Eng. Data* **39**, 330–332 (1994)
- Trémosa, J., Castillo, C., Vong, C.Q., Kervévan, C., Lassin, A., Audigane, P.: Long-term Assessment of Geochemical Reactivity of CO₂ Storage in Highly Saline Aquifers: Application to Ketzin. In Salah and Snøhvit storage sites. *Int. J. Greenh. Gas Control* **20**, 2–26 (2014)
- Velbel, M.A.: Weathering processes of rock-forming minerals. *Min. Assoc. Can. Short Course Handb.* **10**, 67–111 (1984)
- Velbel, M. A.: Influence of surface area, surface characteristics, and solution composition on feldspar weathering rates. In *Geochemical Processes at Mineral Surfaces*, Am. Chem. Soc. Symp. Series No. 323, 615–634 (1986)
- Verma, A., Pruess, K.: Thermohydrological conditions and silica redistribution near high-level nuclear wastes emplaced in saturated geological formations. *J. Geophys. Res.* **93**, 1159–1173 (1988)
- Voltattorni, N., Sciarra, A., Caramanna, G., Cinti, D., Pizzino, L., Quattrocchi, F.: Gas geochemistry of natural analogues for the studies of geological CO₂ sequestration. *App. Geochem.* **24**(7), 1339–1346 (2009)
- Wang, L.S., Lang, Z.X., Guo, T.M.: Measurement and correlation of the diffusion coefficients of carbon dioxide in liquid hydrocarbon under elevated pressures. *Fluid Phase Equilib.* **117**, 364–372 (1996)
- Witherspoon, P.A., Wang, J.S.Y., Iwai, K., Gale, J.E.: Validity of cubic law for fluid flow in a deformable rock fracture. *Water Resour. Res.* **16**:1016–1024 (1980)
- Witherspoon, P.A., Wang, J.S.Y., Iwai, K., Gale, J.E.: Validity of cubic law for fluid flow in a deformable rock fracture. *Water Resour. Res.* **16**(6), 1016–1024 (2010)
- Weir, G.J., White, S.P., Kissling, W.M.: Reservoir storage and containment of greenhouse gases. In K. Pruess (eds.), *Proceedings of the TOUGH Workshop '95*, Lawrence Berkeley National Laboratory Report LBL-37200, pp. 233–238, Berkeley (1995)
- Wilson, M.J.: Chemical weathering of some primary rock forming minerals. *Soil Sci.* **119**, 349–355 (1975)
- White, A.F., Peterson, M.L.: Role of reactive-surface- area characterization in geochemical kinetic models. In: Melchior, D.C., Bassett, R.L. (eds.), *Chemical Modeling of Aqueous Systems II*. American Chemical Society Symposium Series 416, Washington, DC (Chapter 35), 461–475 (1990)
- Wolery, T.J.: EQ3NR, A computer program for geo- chemical aqueous speciation solubility calculations: theoretical manual, user's guide, and related documentation (Version 7.0). UCRL-MA-110662-PT-III, Lawrence Liver- more National Laboratory, Livermore (1992)
- Worden, R.H.: Dawsonite cement in the Triassic Lam Formation, Shabwa Basin, Yemen: a natural analogue for a potential mineral product of subsurface CO₂ storage for greenhouse gas reduction. *Mar. Pet. Geol.* **23**(1), 61–77 (2006)
- Xu, T., Apps, J.A., Pruess, K.: Numerical simulation of CO₂ disposal by mineral trapping in deep aquifers. *Appl. Geochem.* **19**, 917–936 (2004)
- Xu, T., Apps, J.A., Pruess, K.: Mineral sequestration of carbon dioxide in a sandstone–shale system. *Chem. Geol.* **217**, 295–318 (2005)
- Xu, T., Apps, J.A., Pruess, K., Yamamoto, H.: Numerical modeling of injection and mineral trapping of CO₂ with H₂S and SO₂ in a sandstone formation. *Chem. Geol.* **242**, 319–346 (2007)
- Xu, T., Kharaka, Y.K., Doughty, C.A., Freifeld, B.M., Daley, T.M.: Reactive transport modeling to study changes in water chemistry induced by CO₂ injection at the Frio-I Brine Pilot. *Chem. Geol.* **271**, 153–164 (2010)
- Xu, T., Pruess, K.: Modeling multiphase non-isothermal fluid flow and reactive geochemical transport in variably saturated fractured rocks: 1. methodology. *Am. J. Sci.* **301**, 16–33 (2001)
- Xu, T., Pruess, K., Brimhall, G.: An improved equilibrium-kinetics speciation algorithm for redox reactions in variably saturated subsurface flow system. *Comput. Geosci.* **25**, 655–666 (1999)
- Xu, T., Sonnenthal, E.L., Spycher, N., Pruess, K.: TOUGHREACT: a simulation program for non-isothermal multiphase reactive geochemical transport in variably saturated geologic media. *Comput. Geosci.* **32**, 145–165 (2006)

- Yasuhara, H., Polak, A., Mitani, Y., Halleck, P.M., Elsworth, D.: Evolution of fracture permeability through fluid–rock reaction under hydrothermal conditions. *Earth Planet. Sci. Lett.* **244**(1–2), 186–200 (2006)
- Zerai, B., Saylor, B.Z., Matisoff, G.: Computersimulation of CO₂ trapped through mineral precipitation in the Rose Run Sandstone. *Ohio. Appl. Geochem.* **21**(2), 223–240 (2006)